

1 Stokes flow in a doubly-periodic domain with two walls

We want to solve the Stokes equations,

$$\eta \nabla^2 \mathbf{u} - \nabla p = -\mathbf{f}, \quad (1.1)$$

$$\nabla \cdot \mathbf{u} = 0, \quad (1.2)$$

on a doubly periodic domain $\Omega := (x, y, z) \in [-L, L] \times [-L, L] \times [z_0, z_1]$ subject to *no-slip* boundary conditions (BCs) on the bottom and top walls;

$$\mathbf{u}|_{z=z_0} = \mathbf{u}|_{z=z_1} = 0, \quad (1.3)$$

where $\mathbf{u} = [u \ v \ w]^T$, and $\mathbf{f} = [f \ g \ h]^T$ are Gaussian sources representing particles with an effective hydrodynamic radius of R_h . Specifically, \mathbf{f} consists of monopole and dipole terms with Gaussian force envelopes Δ_f , Δ_τ ;

$$\Delta_f(\mathbf{x}) = \frac{1}{\sqrt{8\pi^3 g_f^6}} \exp\left(-\frac{\|\mathbf{x}\|^2}{2g_f^2}\right), \quad (1.4)$$

$$\Delta_\tau(\mathbf{x}) = \frac{1}{\sqrt{8\pi^3 g_\tau^6}} \exp\left(-\frac{\|\mathbf{x}\|^2}{2g_\tau^2}\right), \quad (1.5)$$

where $g_f = R_h/\sqrt{\pi}$ and $g_\tau = R_h/(6\sqrt{\pi})^{1/3}$. The monopole term represents the force exerted by particles on the fluid, while Δ_τ relates to external torques $\boldsymbol{\tau}$ on the particles, as in

$$\mathbf{f}(\mathbf{x}) = \sum_{k=1}^M \mathbf{f}(\mathbf{y}_k) \Delta_f(\mathbf{x} - \mathbf{y}_k) + \frac{1}{2} \nabla \times (\boldsymbol{\tau}(\mathbf{y}_k) \Delta_\tau(\mathbf{x} - \mathbf{y}_k)) = \mathbf{S}_f \mathcal{F} + \frac{1}{2} \nabla \times (\mathbf{S}_\tau \boldsymbol{\mathcal{T}}), \quad (1.6)$$

where \mathbf{y}_k is the position of particle k [1]. Near the wall, i.e. $z < 4g_f + z_0$, $z > z_1 - 4g_f$, we ensure that the forces and torques decay to 0 by adding the negative of a given particle's Gaussian, centered at the point of its reflection about the wall. That is, we replace Δ_f and Δ_τ in Eq. 1.6 with

$$\Delta^W(\mathbf{x} - \mathbf{y}) = \Delta(\mathbf{x} - \mathbf{y}) - \Delta(\mathbf{x} - \mathbf{y}^{\text{im}}), \quad (1.7)$$

where $\mathbf{y}^{\text{im}} = \mathbf{y} - 2\hat{\mathbf{e}}_z(\hat{\mathbf{e}}_z \cdot \mathbf{y})$ is the particle's reflection about the bottom wall. Once we've solved for the fluid velocity \mathbf{u} , we can obtain the linear and angular velocities of the particles through

$$\mathbf{V}(\mathbf{x}) = \int_{\Omega} \mathbf{u}(\mathbf{y}) \Delta_f(\mathbf{y} - \mathbf{x}) d\mathbf{y} = \mathbf{J}_f \mathbf{U}, \quad (1.8)$$

$$\boldsymbol{\Omega}(\mathbf{x}) = \frac{1}{2} \int_{\Omega} (\nabla \times \mathbf{u}(\mathbf{y})) \Delta_\tau(\mathbf{y} - \mathbf{x}) d\mathbf{y} = \frac{1}{2} \mathbf{J}_\tau (\nabla \times \mathbf{U}), \quad (1.9)$$

while making sure to use the wall envelopes as needed. Near the top wall, the sources are similarly defined.

1.1 Decoupling velocity from pressure

The component-wise Stokes equations in Cartesian coordinates are given by

$$\eta \nabla u^2 - \partial_x p = -f, \quad (1.10)$$

$$\eta \nabla v^2 - \partial_y p = -g, \quad (1.11)$$

$$\eta \nabla w^2 - \partial_z p = -h, \quad (1.12)$$

$$\partial_x u + \partial_y v + \partial_z w = 0. \quad (1.13)$$

Fourier transforming Eqs 1.10 - 1.13 in x and y and applying Fourier derivative relations, we have

$$\eta(k_{\parallel}^2 - \partial_{zz})\hat{u}(\mathbf{k}_{\parallel}, z) + ik_x \hat{p}(\mathbf{k}_{\parallel}, z) = \hat{f}(\mathbf{k}_{\parallel}, z), \quad (1.14)$$

$$\eta(k_{\parallel}^2 - \partial_{zz})\hat{v}(\mathbf{k}_{\parallel}, z) + ik_y \hat{p}(\mathbf{k}_{\parallel}, z) = \hat{g}(\mathbf{k}_{\parallel}, z), \quad (1.15)$$

$$\eta(k_{\parallel}^2 - \partial_{zz})\hat{w}(\mathbf{k}_{\parallel}, z) + \partial_z \hat{p}(\mathbf{k}_{\parallel}, z) = \hat{h}(\mathbf{k}_{\parallel}, z), \quad (1.16)$$

$$ik_x \hat{u}(\mathbf{k}_{\parallel}, z) + ik_y \hat{v}(\mathbf{k}_{\parallel}, z) + \partial_z \hat{w}(\mathbf{k}_{\parallel}, z) = 0, \quad (1.17)$$

$$\hat{\mathbf{u}}(\mathbf{k}_{\parallel}, z = z_0) = \hat{\mathbf{u}}(\mathbf{k}_{\parallel}, z = z_1) = 0, \quad (1.18)$$

where $\mathbf{k}_{\parallel} = [k_x \ k_y]^T$ is the vector of wave numbers in x and y , $k_{\parallel}^2 = \mathbf{k}_{\parallel} \cdot \mathbf{k}_{\parallel}$, and $\hat{\cdot}$ denotes the Fourier transform. Specifically, $k_x, k_y = \frac{2\pi j}{2L}$, $j = -\frac{N}{2}, \dots, \frac{N}{2} - 1$, where N is the number of points in the x and y discretization. We can decouple the velocity from the pressure in Eqs. 1.14 - 1.16 through a series of algebraic manipulations and applications of ∂_z , revealing a linear system and BCs for a new variable $\hat{\chi}$ given by

$$\hat{\mathbf{x}} = \begin{bmatrix} \hat{\chi} \\ \hat{\psi} \\ \hat{w} \end{bmatrix} = \begin{bmatrix} \partial_z \hat{u} \\ \partial_z \hat{v} \\ \hat{w} \end{bmatrix}. \quad (1.19)$$

Ultimately, we integrate $\hat{\chi}$ and $\hat{\psi}$ from z_0 to z to recover \hat{u} and \hat{v} . The steps for the derivation are provided below, where the boxed equations are the decoupled ones we will use.

(i) First, we compute $ik_x \left[\frac{i\partial_z}{k_x} (\text{Eq. 1.14}) + \text{Eq. 1.16} \right]$, resulting in

$$\eta(k_{\parallel}^2 - \partial_{zz})(\hat{\chi} - ik_x \hat{w}) = \partial_z \hat{f} - ik_x \hat{h}. \quad (1.20)$$

(ii) Similarly, we compute $ik_y \left[\frac{i\partial_z}{k_y} (\text{Eq. 1.15}) + \text{Eq. 1.16} \right]$, yielding

$$\eta(k_{\parallel}^2 - \partial_{zz})(\hat{\psi} - ik_y \hat{w}) = \partial_z \hat{g} - ik_y \hat{h}. \quad (1.21)$$

(iii) Next, we observe that Eq. 1.17 implies

$$\boxed{\partial_{zz} \hat{w} = -i(k_x \hat{\chi} + k_y \hat{\psi})} \quad (1.22)$$

(iv) Substituting Eq. 1.22 into Eq. 1.20 gives

$$\boxed{\eta((k_{\parallel}^2 + k_x^2 - \partial_{zz})\hat{\chi} + k_x k_y \hat{\psi} - ik_x k_{\parallel}^2 \hat{w}) = \partial_z \hat{f} - ik_x \hat{h}.} \quad (1.23)$$

(v) Substituting Eq. 1.22 into Eq. 1.21 gives

$$\boxed{\eta((k_{\parallel}^2 + k_y^2 - \partial_{zz})\hat{\psi} + k_x k_y \hat{\chi} - ik_y k_{\parallel}^2 \hat{w}) = \partial_z \hat{g} - ik_y \hat{h}.} \quad (1.24)$$

1.2 Boundary Conditions

After eliminating the pressure, we have 3 equations for 3 variables, and two boundaries. So, we require 6 BCs to complete the problem specification. These can be derived by considering the original BC Eq. 1.18.

- (i) Evaluating Eq. 1.17 at $z = z_0, z_1$ and considering the third component of Eq. 1.18, we have the following 4 BCs for \hat{w} :

$$\hat{w}(\mathbf{k}_{\parallel}, z_0) = 0, \quad (1.25)$$

$$\hat{w}(\mathbf{k}_{\parallel}, z_1) = 0, \quad (1.26)$$

$$\partial_z \hat{w}(\mathbf{k}_{\parallel}, z_0) = 0, \quad (1.27)$$

$$\partial_z \hat{w}(\mathbf{k}_{\parallel}, z_1) = 0. \quad (1.28)$$

- (ii) If we evaluate $[k_y(\text{Eq. 1.14}) - k_x(\text{Eq. 1.15})]$ at $z = z_0, z_1$, we find

$$\eta \partial_z (k_y \hat{\chi}(\mathbf{k}_{\parallel}, z_0) - k_x \hat{\psi}(\mathbf{k}_{\parallel}, z_0)) = k_x \hat{g}(\mathbf{k}_{\parallel}, z_0) - k_y \hat{f}(\mathbf{k}_{\parallel}, z_0), \quad (1.29)$$

$$\eta \partial_z (k_y \hat{\chi}(\mathbf{k}_{\parallel}, z_1) - k_x \hat{\psi}(\mathbf{k}_{\parallel}, z_1)) = k_x \hat{g}(\mathbf{k}_{\parallel}, z_1) - k_y \hat{f}(\mathbf{k}_{\parallel}, z_1). \quad (1.30)$$

Note, if we compute $[k_y(\text{Eq. 1.20}) - k_x(\text{Eq. 1.21})]$, integrate the result from z_0 to z_1 and apply the two conditions above, we see that

$$\begin{aligned} (k_y \hat{f} - k_x \hat{g}) \Big|_{z_0}^{z_1} &= \eta \left(k_{\parallel}^2 \int_{z_0}^{z_1} k_y \hat{\chi} - k_x \hat{\psi} dz \right) + \eta \left(k_x \partial_z \hat{\psi} - k_y \partial_z \hat{\chi} \right) \Big|_{z_0}^{z_1}, \\ &\Rightarrow k_x \int_{z_0}^{z_1} \hat{\psi} dz = k_y \int_{z_0}^{z_1} \hat{\chi} dz. \end{aligned} \quad (1.31)$$

However, integrating Eq. 1.22 and enforcing Eqs. 1.27 - 1.28 yields the relation

$$\int_{z_0}^{z_1} \hat{\psi} dz = -\frac{k_x}{k_y} \int_{z_0}^{z_1} \hat{\chi} dz. \quad (1.32)$$

Inserting this into Eq. 1.31 results in a contradiction unless the integrals are both 0. Thus, BCs Eq. 1.29 - 1.30 correctly imply the parallel velocities are the same on the bottom and top walls.

1.3 Equations for $\mathbf{k}_{\parallel} = 0$

Here, we consider the equations for the simpler case of $\mathbf{k}_{\parallel} = 0$. Of note is that we can directly solve for $\hat{\mathbf{u}}$ and \hat{p} .

1.3.1 \hat{u} and \hat{v}

First, we consider the equations for $\hat{u}(0, z)$. When $\mathbf{k}_{\parallel} = 0$, Eq 1.14 reduces to

$$\partial_{zz} \hat{u}(0, z) = -\frac{\hat{f}(0, z)}{\eta}, \quad (1.33)$$

By integrating twice and applying Eq. 1.18, we find

$$\hat{u}(0, z) = -\frac{1}{\eta} \left[\int_{z_0}^z \left(\int_{z_0}^t \hat{f}(0, \tau) d\tau \right) dt + \frac{z - z_0}{z_0 - z_1} \int_{z_0}^{z_1} \left(\int_{z_0}^t \hat{f}(0, \tau) d\tau \right) dt \right] \quad (1.34)$$

We can evaluate $\hat{u}(0, z)$ easily using the Chebyshev second integral operator \mathcal{J}^2 , described in the next section. An analogous argument holds for $\hat{v}(0, z)$.

1.3.2 \hat{w}

Moving onto the equation for $\hat{w}(0, z)$, Eq. 1.17 reduces to

$$\partial_z \hat{w}(0, z) = 0. \quad (1.35)$$

Since we enforce a no slip BC, we must have

$$\hat{w}(0, z) = 0. \quad (1.36)$$

1.3.3 \hat{p}

If we want to recover the pressure for $\mathbf{k}_{\parallel} = 0$, we substitute Eq. 1.36 into Eq. 1.16 so that

$$\hat{p}(0, z) = \int_{z_0}^z \hat{h}(0, \tau) d\tau, \quad (1.37)$$

where we pin $\hat{p}(0, z)$ to 0 at z_0 .

1.4 Spectral BVP Solver

We can construct a system of integral equations from Eqs 1.22 - 1.24 by solving for the second order terms $\sigma_{\chi}(z) = \partial_{zz}\hat{\chi}$, $\sigma_{\psi}(z) = \partial_{zz}\hat{\psi}$, $\sigma_w(z) = \partial_{zz}\hat{w}$ for fixed \mathbf{k}_{\parallel} instead of $\hat{\chi}$, $\hat{\psi}$ and \hat{w} [2]. For now, suppose $z \in [-1, 1]$. Representing σ_{χ} , \hat{f} by truncated Chebyshev series in vector-dot notation,

$$\begin{aligned} \sigma_{\chi}(z) &\approx \mathbf{a}_{\chi} \cdot \mathbf{T}(z), & \partial_z \hat{\chi} &\approx \mathbf{d}_{\chi} \cdot \mathbf{T}(z), & \hat{\chi} &\approx \mathbf{c}_{\chi} \cdot \mathbf{T}(z), \\ \partial_z \hat{f}(z) &\approx \mathbf{d}_f \cdot \mathbf{T}(z), & \hat{f}(z) &\approx \mathbf{c}_f \cdot \mathbf{T}(z), \end{aligned} \quad (1.38)$$

and doing the same for the analogous variables, we can rewrite the system as

$$0 = ik_x \mathbf{c}_{\chi} + ik_y \mathbf{c}_{\psi} + \mathbf{a}_w \quad (1.39)$$

$$(\mathbf{d}_f - ik_x \mathbf{c}_h) = -\eta \mathbf{a}_{\chi} + \alpha_1 \mathbf{c}_{\chi} + \beta \mathbf{c}_{\psi} + \gamma_1 \mathbf{c}_w \quad (1.40)$$

$$(\mathbf{d}_g - ik_y \mathbf{c}_h) = \beta \mathbf{c}_{\chi} - \eta \mathbf{a}_{\psi} + \alpha_2 \mathbf{c}_{\psi} + \gamma_2 \mathbf{c}_w, \quad (1.41)$$

where the constants

$$\alpha_1 = \eta(k_{\parallel}^2 + k_x^2), \quad \alpha_2 = \eta(k_{\parallel}^2 + k_y^2), \quad \beta = \eta k_x k_y, \quad \gamma_1 = -i\eta k_x k_{\parallel}^2, \quad \gamma_2 = -i\eta k_y k_{\parallel}^2. \quad (1.42)$$

Note that for even sized grids, care must be taken to zero out the unpaired mode in the constants that resulted from first derivatives in Fourier space, namely for all terms except k_{\parallel}^2 (we actually just ignore this unmatched mode). Also, in practice, we use Chebyshev interpolants as their coefficients can be computed in $\mathcal{O}(N_z \log(N_z))$ time using the FFT, rather than evaluating the coefficients in the truncated series by integration. All vectors are of length N_z , which is the number of Chebyshev points. Now, consider \mathcal{J}^2 , the Chebyshev second integral mapping (from Ondrej's notes), which relates \mathbf{c} to \mathbf{a} by

$$\begin{aligned} c_1 &= d_0 - \frac{1}{8}(a_1 - a_3) \\ c_2 &= \frac{a_0}{2} - \frac{a_2}{6} + \frac{a_4}{24} \\ c_n &= \frac{1}{2n-2} \left(\frac{1}{2n-2}(a_{n-2} - a_n) - \frac{1}{2n+2}(a_n - a_{n+2}) \right), \quad n \geq 3, \end{aligned} \quad (1.43)$$

where $n = 0, 1, \dots, N - 1$ and c_0, d_0 are free parameters. Inserting Eq. 1.43 into Eqs. 1.39 - 1.41, we find the following underdetermined block-linear system;

$$\begin{pmatrix} 0 \\ \mathbf{d}_f - ik_x \mathbf{c}_h \\ \mathbf{d}_g - ik_y \mathbf{c}_h \end{pmatrix} = \begin{pmatrix} ik_x \mathcal{J}^2 & ik_y \mathcal{J}^2 & \mathbf{I} \\ -\eta \mathbf{I} + \alpha_1 \mathcal{J}^2 & \beta \mathcal{J}^2 & \gamma_1 \mathcal{J}^2 \\ \beta \mathcal{J}^2 & -\eta \mathbf{I} + \alpha_2 \mathcal{J}^2 & \gamma_2 \mathcal{J}^2 \end{pmatrix} \begin{pmatrix} \mathbf{a}_\chi \\ \mathbf{a}_\psi \\ \mathbf{a}_w \end{pmatrix} + \begin{pmatrix} ik_x & ik_y & 0 & 0 & 0 & 0 \\ 0 & 0 & 0 & ik_x & ik_y & 0 \\ \vdots & & \ddots & & & \\ \alpha_1 & \beta & \gamma_1 & 0 & 0 & 0 \\ 0 & 0 & 0 & \alpha_1 & \beta & \gamma_1 \\ \vdots & & \ddots & & & \\ \beta & \alpha_2 & \gamma_2 & 0 & 0 & 0 \\ 0 & 0 & 0 & \beta & \alpha_2 & \gamma_2 \\ \vdots & & \ddots & & & \end{pmatrix} \begin{pmatrix} c_\chi^0 \\ c_\psi^0 \\ c_w^0 \\ d_\chi^0 \\ d_\psi^0 \\ d_w^0 \end{pmatrix},$$

$$\Rightarrow \mathbf{F} = \mathbf{A}\mathbf{U}_a + \mathbf{B}\mathbf{U}_b. \quad (1.44)$$

At this point, we have $3N$ equations for $3N+6$ unknowns. The BCs Eqs. 1.25 - 1.30 take the form;

$$\mathbf{c}_w \cdot \mathbf{T}(z_0) = 0, \quad (1.45)$$

$$\mathbf{c}_w \cdot \mathbf{T}(z_1) = 0, \quad (1.46)$$

$$\mathbf{d}_w \cdot \mathbf{T}(z_0) = 0, \quad (1.47)$$

$$\mathbf{d}_w \cdot \mathbf{T}(z_1) = 0, \quad (1.48)$$

$$\eta(k_y \mathbf{d}_\chi - k_x \mathbf{d}_\psi) \cdot \mathbf{T}(z_0) = (k_x \mathbf{c}_g - k_y \mathbf{c}_f) \cdot \mathbf{T}(z_0), \quad (1.49)$$

$$\eta(k_y \mathbf{d}_\chi - k_x \mathbf{d}_\psi) \cdot \mathbf{T}(z_1) = (k_x \mathbf{c}_g - k_y \mathbf{c}_f) \cdot \mathbf{T}(z_1), \quad (1.50)$$

which yields 6 additional rows to Eq. 1.44;

$$\begin{pmatrix} (k_x \mathbf{c}_g - k_y \mathbf{c}_f) \cdot \mathbf{T}(z_0) \\ (k_x \mathbf{c}_g - k_y \mathbf{c}_f) \cdot \mathbf{T}(z_1) \\ 0 \\ 0 \\ 0 \\ 0 \end{pmatrix} = \begin{pmatrix} \eta k_y \mathbf{T}(z_0) \cdot \mathcal{J} & -\eta k_x \mathbf{T}(z_0) \cdot \mathcal{J} \\ \eta k_y \mathbf{T}(z_1) \cdot \mathcal{J} & -\eta k_x \mathbf{T}(z_1) \cdot \mathcal{J} \\ & \mathbf{T}(z_0) \cdot \mathcal{J}^2 \\ & \mathbf{T}(z_1) \cdot \mathcal{J}^2 \\ & \mathbf{T}(z_0) \cdot \mathcal{J} \\ & \mathbf{T}(z_1) \cdot \mathcal{J} \end{pmatrix} \mathbf{U}_a$$

$$+ \begin{pmatrix} 0 & 0 & 0 & \eta k_y T_0(z_0) & -\eta k_x T_0(z_0) & 0 \\ 0 & 0 & 0 & \eta k_y T_0(z_1) & -\eta k_x T_0(z_1) & 0 \\ 0 & 0 & T_0(z_0) & 0 & 0 & T_1(z_0) \\ 0 & 0 & T_0(z_1) & 0 & 0 & T_1(z_1) \\ 0 & 0 & 0 & 0 & 0 & T_0(z_0) \\ 0 & 0 & 0 & 0 & 0 & T_0(z_1) \end{pmatrix} \mathbf{U}_b, \quad (1.51)$$

$$\Rightarrow \mathbf{F}_{bc} = \mathbf{C}\mathbf{U}_a + \mathbf{D}\mathbf{U}_b,$$

where \mathcal{J} is the Chebyshev first integral mapping, which relates \mathbf{d} to \mathbf{a} by

$$\begin{aligned} d_1 &= \frac{1}{2}(2a_0 - a_2) \\ d_n &= \frac{1}{2n}(a_{n-1} - a_{n+1}), \quad n > 1. \end{aligned} \quad (1.52)$$

Altogether, we have the following block system of $3N + 6$ equations for $3N + 6$ unknowns;

$$\begin{pmatrix} \mathbf{F} \\ \mathbf{F}_{bc} \end{pmatrix} = \begin{pmatrix} \mathbf{A} & \mathbf{B} \\ \mathbf{C} & \mathbf{D} \end{pmatrix} \begin{pmatrix} \mathbf{U}_a \\ \mathbf{U}_b \end{pmatrix}, \quad (1.53)$$

where \mathbf{A} is $3N \times 3N$ with 8 pentadiagonal and 1 diagonal blocks, \mathbf{B} is $3N \times 6$, \mathbf{C} is $6 \times 3N$ and \mathbf{D} is 6×6 . We can use the same Schur complement approach given in Ondrej's notes to solve for $\mathbf{U}_a, \mathbf{U}_b$ (system is invertible $\forall \mathbf{k}_{\parallel} \neq 0$). Additionally, if we reorder the unknowns so that the coefficients of $\sigma_{\chi}, \sigma_{\psi}, \sigma_w$ at a given z are right after one another, \mathbf{A} ends up block tri-diagonal, and MATLAB's banded solver (no separate LU) activated via backslash on sparse arguments will do the job. In fact, permuting the system significantly reduces the solve time for greater numbers of Chebyshev points.

If $z \in [z_0, z_1] \neq [-1, 1]$, the first and second integral mappings are multiplied by H and H^2 , respectively, where $H = (z_1 - z_0)/2$. Moreover, shifted Chebyshev polynomials should be used when needed - the Clenshaw-Curtis points $\tilde{z} \in [-1, 1]$ should be linearly rescaled with

$$z = H\tilde{z} + \frac{z_1 + z_0}{2}, \quad (1.54)$$

and the weights multiplied by H . The matrices \mathbf{A} and \mathbf{B} are returned as one through the routine `secondCoupledIntegralMatrix`, which takes as input $\mathcal{J}^2, \eta, k_x, k_y$ and H . Similarly, matrices \mathbf{C} and \mathbf{D} are returned from the routine `twoWallBCRows`, which takes $N_z, H, \mathbf{T}, \mathcal{J}, \mathcal{J}^2, \eta, k_x, k_y$. Then, we pass $[\mathbf{A}, \mathbf{B}], [\mathbf{C}, \mathbf{D}], \mathbf{F}, \mathbf{F}_{bc}$ and forward/backward permutation vectors `fperm` and `bperm` to the routine `coupledBVPChebInt` to solve for \mathbf{U}_a and \mathbf{U}_b .

1.4.1 $\mathbf{k}_{\parallel} = \mathbf{0}$

From Eq. 1.34, it is clear that we can apply \mathcal{J}^2 to \mathbf{c}_f to get the Chebyshev coefficients \mathbf{c}_u of \hat{u} . However, we must take care to set the integration constants c_u^0, d_u^0 properly. For generality, we consider arbitrary z_0 and z_1 and shifted polynomials. Let $H = (z_1 - z_0)/2$. Then, we can fully determine \mathbf{c}_u (and \mathbf{c}_v analogously) by solving

$$\begin{pmatrix} \mathbf{I} & 0 & 0 \\ H^2 \mathbf{T}(z_0) \cdot \mathcal{J}^2 & H^2 T_0(z_0) & H^2 T_1(z_0) \\ H^2 \mathbf{T}(z_1) \cdot \mathcal{J}^2 & H^2 T_0(z_1) & H^2 T_1(z_1) \end{pmatrix} \begin{pmatrix} \mathbf{a}_u \\ c_u^0 \\ d_u^0 \end{pmatrix} = \begin{pmatrix} -\frac{1}{\eta} \mathbf{c}_f \\ 0 \\ 0 \end{pmatrix}, \quad (1.55)$$

and computing \mathbf{c}_u/H^2 with the forward map in Eq. 1.43.

We can recover the coefficients \mathbf{c}_p of \hat{p} by computing $\mathbf{c}_p = H\mathcal{J}\mathbf{c}_h$ and pinning $\hat{p}(0, z_0) = 0$ by setting

$$c_p^0 = \sum_{j=1}^{N-1} (-1)^{j+1} c_p^j, \quad (1.56)$$

as indicated in Section 1.3.3.

1.5 Recovering coefficients of \hat{u}, \hat{v} and \hat{p} for $\mathbf{k}_{\parallel} \neq 0$

Once we have the coefficients $\mathbf{a}_{\chi}, c_{\chi}^0$ and d_{χ}^0 , we can use \mathcal{J}^2 to compute \mathbf{c}_{χ} . Then, the uncorrected (constant offset) coefficients of \hat{u} are $\mathbf{c}_u = \mathcal{J}\mathbf{c}_{\chi}$, with $c_u^0 = 0$. Since Eqs. 1.31 - 1.32 imply the values of \hat{u} at the endpoints are equal, the correction amounts to

$$\hat{u}(z) \rightarrow \hat{u}(z) - \hat{u}(z_1) = (\mathbf{T}(z) - \mathbf{T}(z_1)) \cdot \mathbf{c}_u, \quad (1.57)$$

which is equivalent to setting

$$c_u^0 = -\mathbf{T}(z_1) \cdot \mathbf{c}_u = -\sum_{j=1}^{N-1} c_u^j. \quad (1.58)$$

An analogous correction is made for the coefficients of \hat{v} .

1.5.1 \hat{p}

After applying Chebyshev expansions using the same notation indicated in [Eq. 1.38](#) onto [Eq. 1.16](#), we can recover the coefficients of the pressure derivative with

$$\mathbf{d}_p = \mathbf{c}_h - \eta(k_{\parallel}^2 \mathbf{c}_w - \mathbf{a}_w), \quad (1.59)$$

so that the uncorrected coefficients of \hat{p} are $\mathbf{c}_p = \mathcal{J}\mathbf{d}_p$, with $c_p^0 = 0$. To determine c_p^0 , we consider the zero Chebyshev mode of either [Eq. 1.14](#) or [Eq. 1.15](#), depending on whether k_y or k_x is 0 and find that

$$\begin{aligned} c_p^0 &= \frac{1}{ik_x} (c_f^0 - \eta(k_{\parallel}^2 c_u^0 - d_{\chi}^0)), \text{ if } k_y = 0 \\ c_p^0 &= \frac{1}{ik_y} (c_g^0 - \eta(k_{\parallel}^2 c_v^0 - d_{\psi}^0)), \text{ if } k_x = 0. \end{aligned} \quad (1.60)$$

It has been confirmed numerically that the two equations give the same constants when k_y and k_x are both non-zero, so we take their average in such case.

2 Stokes flow in a doubly-periodic domain with a bottom wall

Here, we consider the bottom wall geometry, i.e. doubly periodic in x and y with z bounded below only. As before, we have no slip BCs at $z = z_0$. At $z = z_1$, we derive three new equations to enforce an open BC.

2.1 Open BCs at $z = z_1$

See the Maple worksheet for more details, wherein Ondrej's general solution for $z > z_1$ was used to determine the BCs. They are;

$$0 = [\partial_z \hat{\chi} + k_{\parallel} \hat{\chi} - ik_x (\partial_z \hat{w} + k_{\parallel} \hat{w})]_{z_1}, \quad (2.1)$$

$$0 = [\partial_z \hat{\psi} + k_{\parallel} \hat{\psi} - ik_y (\partial_z \hat{w} + k_{\parallel} \hat{w})]_{z_1}, \quad (2.2)$$

$$0 = [ik_x \hat{\chi} + ik_y \hat{\psi} - 2k_{\parallel} (\partial_z \hat{w} + \frac{k_{\parallel} \hat{w}}{2})]_{z_1}. \quad (2.3)$$

So, instead of [Eq. 1.46](#), [Eq. 1.48](#) and [Eq. 1.50](#), we have

$$0 = (\mathbf{d}_{\chi} + k_{\parallel} \mathbf{c}_{\chi} - ik_x (\mathbf{d}_w + k_{\parallel} \mathbf{c}_w)) \cdot \mathbf{T}(z_1), \quad (2.4)$$

$$0 = (\mathbf{d}_{\psi} + k_{\parallel} \mathbf{c}_{\psi} - ik_y (\mathbf{d}_w + k_{\parallel} \mathbf{c}_w)) \cdot \mathbf{T}(z_1), \quad (2.5)$$

$$0 = (ik_x \mathbf{c}_{\chi} + ik_y \mathbf{c}_{\psi} - 2k_{\parallel} (\mathbf{d}_w + \frac{k_{\parallel} \mathbf{c}_w}{2})) \cdot \mathbf{T}(z_1), \quad (2.6)$$

which we obtain through the routine `bottomWallBCRows`.

2.2 $\mathbf{k}_{\parallel} = \mathbf{0}$

The BC equations we previously had for $\mathbf{k}_{\parallel} = \mathbf{0}$ used the no-slip condition at z_1 . Here, we derive new equations to enforce open BCs at z_1 , relying on the fact that solutions are bounded at $+\infty$.

2.2.1 \hat{u} and \hat{v}

In the far field $z \geq z_1$, the force $\mathbf{f} = 0$, which implies $\partial_{zz} \hat{u} = 0$. From boundedness at $+\infty$, we must have $\hat{u}(0, z \geq z_1) = A_u$ and

$$\partial_z \hat{u}(0, z_1) = 0. \quad (2.7)$$

So, the first component of [Eq. 1.18](#) at $\mathbf{k}_{\parallel} = \mathbf{0}$ and [Eq. 2.7](#) are BCs to solve [Eq. 1.33](#) with $z \in [z_0, z_1]$. An analogous argument can be used for $\hat{v}(0, z)$. In our Chebyshev discretization, we enforce [Eq. 2.7](#) by replacing the last row of the matrix and RHS in [Eq. 1.55](#) so that

$$\begin{pmatrix} \mathbf{I} & 0 & 0 \\ H^2 \mathbf{T}(z_0) \cdot \mathcal{J}^2 & H^2 T_0(z_0) & H^2 T_1(z_0) \\ H \mathbf{T}(z_1) \cdot \mathcal{J} & 0 & H T_0(z_1) \end{pmatrix} \begin{pmatrix} \mathbf{a}_u \\ c_u^0 \\ d_u^0 \end{pmatrix} = \begin{pmatrix} -\frac{1}{\eta} \mathbf{c}_f \\ 0 \\ 0 \end{pmatrix}, \quad (2.8)$$

and compute \mathbf{c}_u / H^2 using [Eq. 1.43](#). An analogous approach applies for \mathbf{c}_v .

2.2.2 \hat{w} and \hat{p}

See [Sections 1.3.2 - 1.3.3](#).

2.3 Recovering coefficients of \hat{u}, \hat{v} for $\mathbf{k}_{\parallel} \neq 0$

For both variables, we need only make sure that they are 0 at z_0 . That is, after computing $\mathbf{c}_u = \mathcal{J} c_\chi$ with $c_u^0 = 0$, we set

$$c_u^0 = \sum_{j=1}^{N-1} (-1)^{j+1} c_u^j, \quad (2.9)$$

and do the same for \mathbf{c}_v .

3 Implementation Details

Here, we provide a brief description of the pre- and post-computations that wrap around the solution procedure explicated in the previous sections.

3.1 Pre-processing

Once we've defined parameters such as $R_h, g_f, g_\tau, \eta, L, z_0, z_1$, the grids in x and y , the Chebyshev nodes/weights, wave numbers k_x, k_y , locations of the particles in the domain (and their images if necessary), and the forces/torques on the particles, we precompute the following:

- (1) Shifted Chebyshev polynomials $\mathbf{T}(z)$ using the function `chebPoly`, which takes as inputs a column vector of the Chebyshev nodes and N_T , corresponding to the number of polynomials we want. In our case, $N_T = N_z$.
- (2) Integral operators \mathcal{J} and \mathcal{J}^2 .
- (3) Forward and backward permutation vectors `fperm` and `bperm` for reordering unknowns in [Eq. 1.53](#) to yield a block tri-diagonal system.
- (4) Spreading matrices $\mathbf{S}_f, \mathbf{S}_\tau$ and the corresponding interpolation matrices $\mathbf{J}_f, \mathbf{J}_\tau$, formally given in [Eq. 1.6](#) and [Eqs. 1.8 - 1.9](#). This is done by calling the functions `SpreadWts` and `spread`, the latter of which yields the distribution of forces and torques on the grid.
- (5) Fourier and Chebyshev coefficients of the force and torque components f, g, h, τ, v, ϕ using the routine `ftransform`. For later reference, we denote these as \mathbf{C}_F and \mathbf{C}_T , where we use capital letters to indicate the quantities are defined for all wave numbers and Chebyshev points.
- (6) Chebyshev coefficients of $\partial_z \hat{f}, \partial_z \hat{g}, \partial_z \hat{\tau}, \partial_z \hat{v}$ using the routine `chebCoeffDiff`.
- (7) The Fourier and Chebyshev coefficients of the curl term in [Eq. 1.6](#) are evaluated using the already computed coefficients through the relation

$$\frac{1}{2} \nabla \times \mathbf{C}_T = \frac{1}{2} \begin{pmatrix} ik_x \\ ik_y \\ \partial_z \end{pmatrix} \times \begin{pmatrix} \mathbf{C}_\tau \\ \mathbf{C}_v \\ \mathbf{C}_\phi \end{pmatrix} = \frac{1}{2} \begin{pmatrix} ik_y \mathbf{C}_\phi - \mathbf{D}_v \\ \mathbf{D}_\tau - ik_x \mathbf{C}_\phi \\ ik_x \mathbf{C}_v - ik_y \mathbf{C}_\tau \end{pmatrix}. \quad (3.1)$$

- (8) The z -derivatives of the first two components in [Eq. 3.1](#) are obtained by passing them to `chebCoeffDiff`. These appear in, for example, [Eqs. 1.40 - 1.41](#).

3.2 Post-processing

After solving for the Chebyshev coefficients of the fluid velocity \mathbf{u} at a given wave number, we evaluate the local fluid vorticity, i.e. the curl term in Eq. 1.9 spectrally as

$$\frac{1}{2} \nabla \times \mathbf{c}_u = \frac{1}{2} \begin{pmatrix} ik_y \mathbf{c}_w - \mathbf{c}_\psi \\ \mathbf{c}_\chi - ik_x \mathbf{c}_w \\ ik_x \mathbf{c}_v - ik_y \mathbf{c}_u \end{pmatrix}. \quad (3.2)$$

We do this for each wave number instead of at the end so that we don't have to save the intermediate variables $\mathbf{c}_\chi, \mathbf{c}_\psi$. Then, once we've traversed all wave numbers, we perform the following post-computations:

- (1) Compute the values of the linear and angular velocities on the grid in real space by passing the Fourier/Chebyshev coefficients to the routine `btransform`.
- (2) Use the precomputed interpolation matrices $\mathbf{J}_f, \mathbf{J}_\tau$ to evaluate the integrals in Eqs. 1.8 - 1.9 by passing the matrices and linear/angular fluid velocities on the grid to `interpolate`. Note that when particles are near the wall, we pass $\mathbf{J}_f - \mathbf{J}_f^{\text{im}}$ and $\mathbf{J}_\tau - \mathbf{J}_\tau^{\text{im}}$ to the `interpolate` routine. This gives us the linear and angular velocities of the particles.

4 Numerical Validation in Bounded Geometries

After carefully verifying the correctness of our implementation by ensuring that the residuals of the equations in real space converge spectrally to $\varepsilon_{\text{mach}}$ as the number of Chebyshev points is increased, we now turn to validating the code against theoretical predictions on the translational mobility in the two-wall and bottom-wall geometries, as well as the rotational-translational coupling in the latter geometry.

4.1 Single particle translational mobility in the two-wall geometry

Faxen computed power series expansions for the parallel mobility of a particle at half and quarter channel locations, given by

$$\begin{aligned}\mu_{\parallel}(H = \frac{L}{2}) &= \frac{1}{6\pi\eta R_h} \left[1 - 1.004 \frac{R_h}{H} + 0.418 \left(\frac{R_h}{H} \right)^3 + 0.21 \left(\frac{R_h}{H} \right)^4 - 0.169 \left(\frac{R_h}{H} \right)^5 + \dots \right], \\ \mu_{\parallel}(H = \frac{L}{4}) &= \frac{1}{6\pi\eta R_h} \left[1 - 0.6526 \frac{R_h}{H} + 0.1475 \left(\frac{R_h}{H} \right)^3 - 0.131 \left(\frac{R_h}{H} \right)^4 - 0.0644 \left(\frac{R_h}{H} \right)^5 + \dots \right],\end{aligned}\quad (4.1)$$

where H is the height above the bottom wall, $R_h = g_w\sqrt{\pi}$ is the effective hydrodynamic radius of the particle, and L is the channel width. The parallel component of the mobility, μ_{\parallel} is the parallel velocity of the particle (u or v) induced by a unit force in the parallel directions. The perpendicular component of the mobility, μ_{\perp} is analogously computed with the exception that a unit force is prescribed in the perpendicular direction. The test and results are summarized [Figure 1](#), where FCM denotes our solver, based on the force coupling method, and IBM denotes the immersed-boundary method with a 6pt kernel.

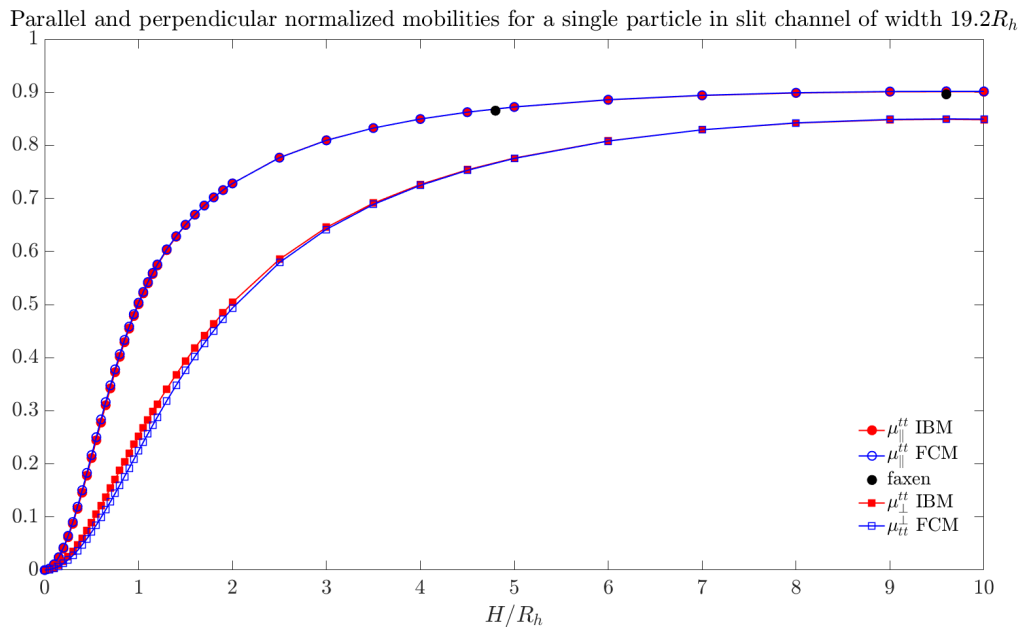


Figure 1: Single particle mobility test in the two-wall geometry with no-slip BCs on the top and bottom walls. The domain was of size $(76.8 \times 76.8 \times 19.2)R_h$ with 128 points in x, y and 128 Chebyshev points in z . Our simulation is in good agreement with the results by Faxen and also matches well to the IBM results.

4.2 Single particle mobility in the bottom-wall geometry

Away from the wall, we use a truncated power series expansion by Faxen for the parallel translational mobility. It is given in [3] as

$$\mu_{\parallel}^{tt}(H) = \frac{1}{6\pi\eta R_h} \left[1 - \frac{9R_h}{16H} + \frac{1}{8} \left(\frac{R_h}{H} \right)^3 - \frac{45}{256} \left(\frac{R_h}{H} \right)^4 - \frac{1}{16} \left(\frac{R_h}{H} \right)^5 + \dots \right]. \quad (4.2)$$

For the perpendicular translational mobility, we use an approximation to an exact series by Brenner, given in [4] as

$$\mu_{\perp}^{tt}(H) = \frac{1}{6\pi\eta R_h} \left[\frac{6 \left(\frac{H'}{R_h} \right)^2 + 2 \left(\frac{H'}{R_h} \right)}{6 \left(\frac{H'}{R_h} \right)^2 + 9 \left(\frac{H'}{R_h} \right) + 2} \right], \quad (4.3)$$

where $H' = H - R_h$ is the distance between the wall and the particle surface. Note that both formulas are for an unbounded half-space, whereas we employ periodic boundaries. The results of the test are summarized in Figure 2;

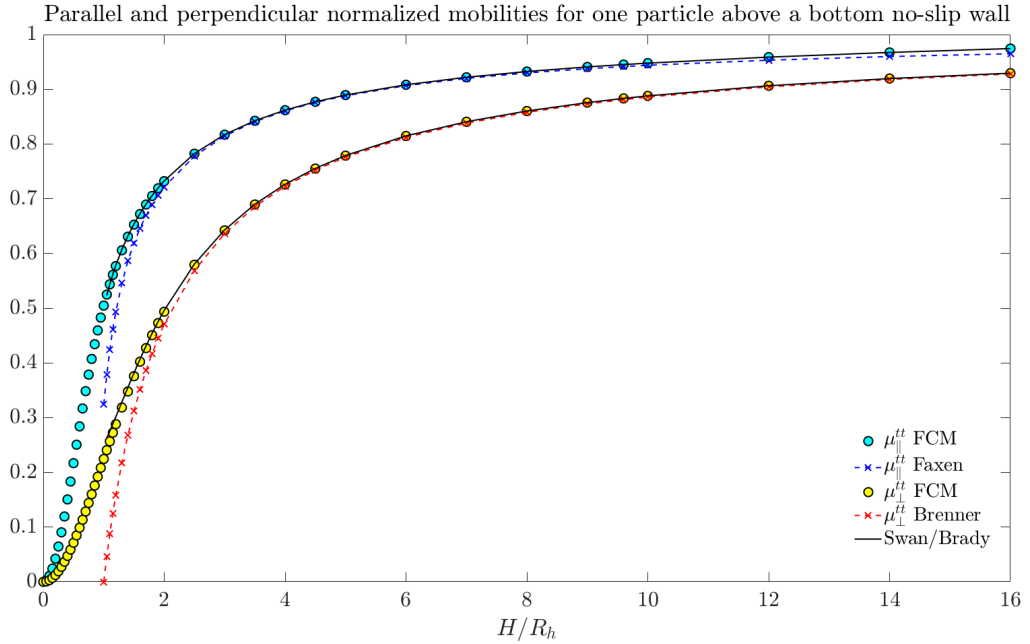


Figure 2: Single particle mobility test in the bottom-wall geometry with no-slip BCs on the bottom wall. The domain was of size $(100 \times 100 \times 19.2)R_h$ with 200 points in x, y, z for both the parallel and perpendicular tests. Our simulation is in good agreement with the results by Faxen and Brenner. The black lines correspond to formulas by Swan and Brady, described in the next section. While these are for an unbounded halfspace, we use 400 images in x and y to reduce the discrepancy with our doubly periodic FCM results.

Next, we consider the rotation-rotation and translation-rotation coupling for a single particle in the bottom wall geometry. The results, summarized in the following figure, are compared to theoretical formulas by Swan and Brady [5], described in the next section. Note, these formulas are also for an unbounded half-space and use a delta function on the surface of the sphere, instead of our doubly-periodic domain with Gaussian kernels. However, we try and reduce the discrepancy by incorporating the effect of 400 images in x and y into the calculation of mobilities using the Swan/Brady formulas.

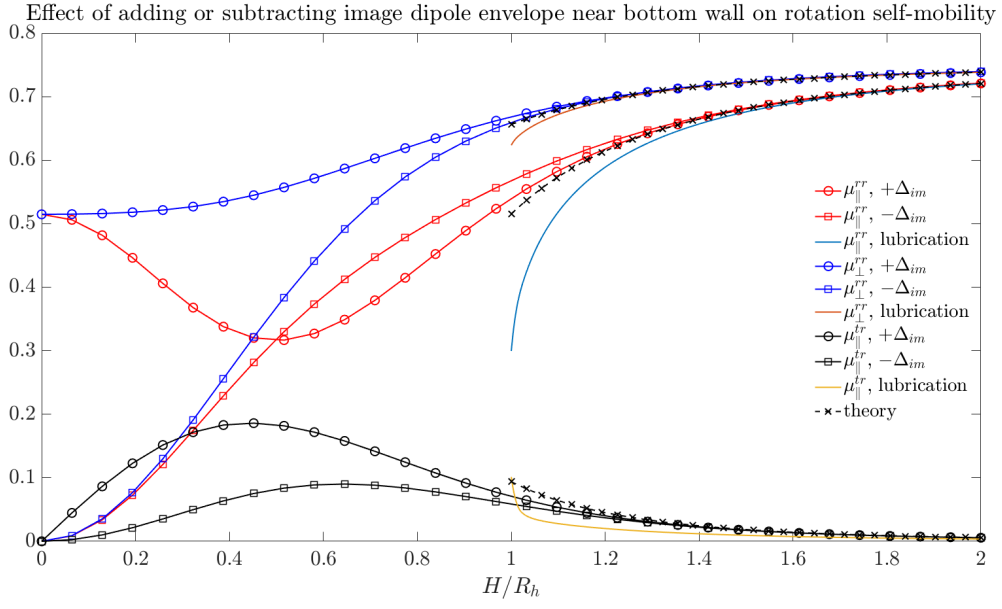


Figure 3: Single particle rotation-rotation and translation-rotation coupling in the bottom-wall geometry with no-slip BCs on the bottom wall. The domain was of size $(100 \times 100 \times 19.2)R_h$ with 200 points in x, y, z for all tests. Our simulation is in good agreement with the direct formulas of Swan and Brady, described in the next section, for $H/R_h > 1$. Circle markers result from adding the image of the dipole kernel near the wall, while square markers correspond to subtraction. The “lubrication” lines are results from lubrication theory for the self-mobility of a sphere above a wall.

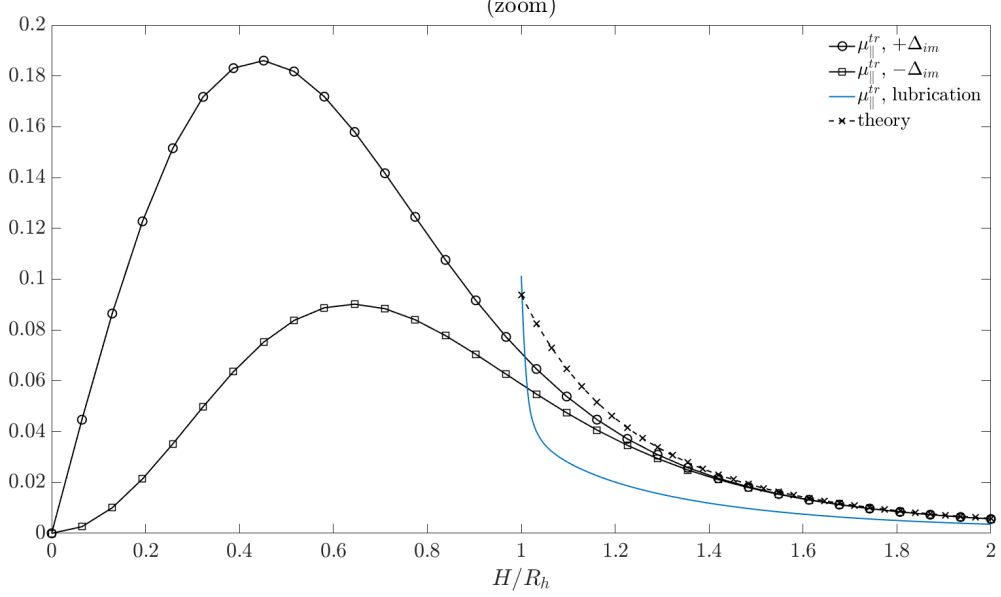


Figure 4: Zoom on the translation-rotation coupling from the previous figure.

4.3 Particle pair mobility in the bottom-wall geometry

Swan and Brady provide explicit formulas relating the moments of the velocity (linear, angular) of particles, relative to the fluid, to those of the force distributions of the particles (force, torque) as in

$$\begin{pmatrix} \mathbf{U} \\ \boldsymbol{\Omega} \end{pmatrix} = \underbrace{\begin{pmatrix} \mathbf{M}^{tt} & \mathbf{M}^{tr} \\ \mathbf{M}^{rt} & \mathbf{M}^{rr} \end{pmatrix}}_{\mathcal{M}} \begin{pmatrix} \mathbf{F} \\ \mathbf{T} \end{pmatrix}, \quad (4.4)$$

which we will use to compute the mobilities of particle q_2 when particle q_1 is prescribed either a force or a torque directed parallel or perpendicular to the wall and compare it to those obtained from our implementation.

We denote certain elements of the matrices appearing in Eq. 4.4 by μ_{ab}^{AB} , which are obtained by applying a unit “ B ” (force/t or torque/r) on q_1 in the a direction and measuring the “ A ” (linear/t or angular/r velocity) of q_2 in the b direction. The formulas are for an unbounded half-space and delta function force envelopes, while we employ periodic boundaries and Gaussians. While we don’t expect perfect matches, we try and reduce the discrepancy, particularly for translation-translation and translation-rotation mobilities away from the wall, by incorporating the effect of 400 images in x and y into the calculation of mobilities using the Swan/Brady formulas. As in the previous test, we use a domain of size $(100 \times 100 \times 19.2)R_h$.

4.3.1 Translational-Translational coupling

To calculate μ_{xx}^{tt} , we prescribe on q_1 a unit force in the x -direction and measure the induced u -velocity of q_2 . For μ_{xz}^{tt} , we apply the same force on q_1 and measure the induced w -velocity of q_2 . Lastly, for μ_{zz}^{tt} , we put a unit force on q_1 in the z -direction and measure the w -velocity of q_2 . The particles are at the same heights and separated by a distance of $3a$, $4a$ or $8a$. We perform these calculations for several heights.

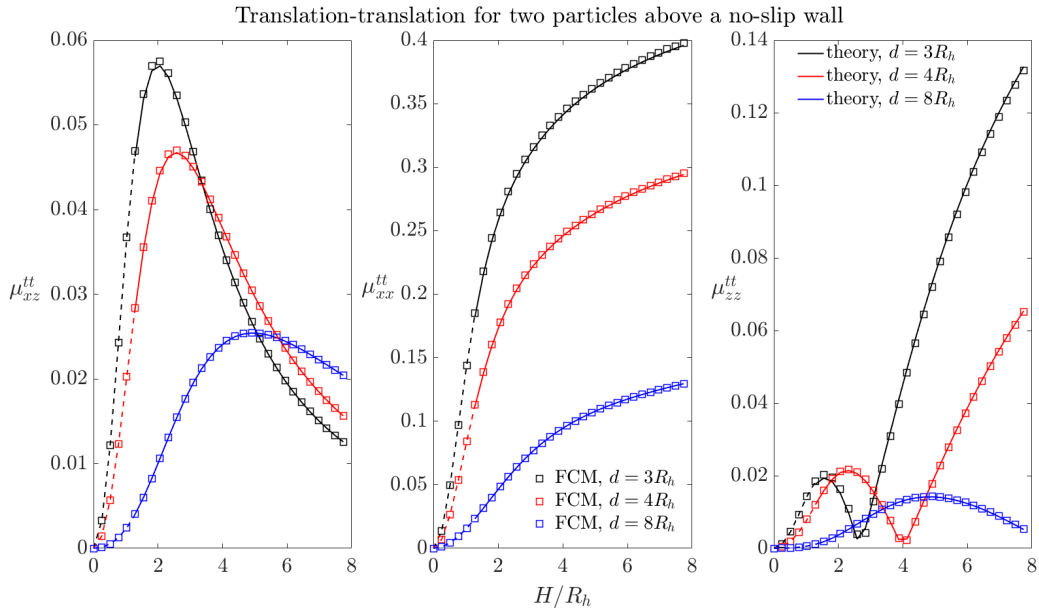


Figure 5: The effect on q_2 ’s linear velocity given a unit force on q_1 . The solid lines correspond to the direct formulas of Swan and Brady. The open square markers are the results from our simulation, which used 128 points in x , y and z . We are in reasonable agreement with the theoretical predictions.

4.3.2 Translational-Rotational coupling

We use the same setup as in the previous section, except we apply unit torques on q_1 and measure the velocities of q_2 .

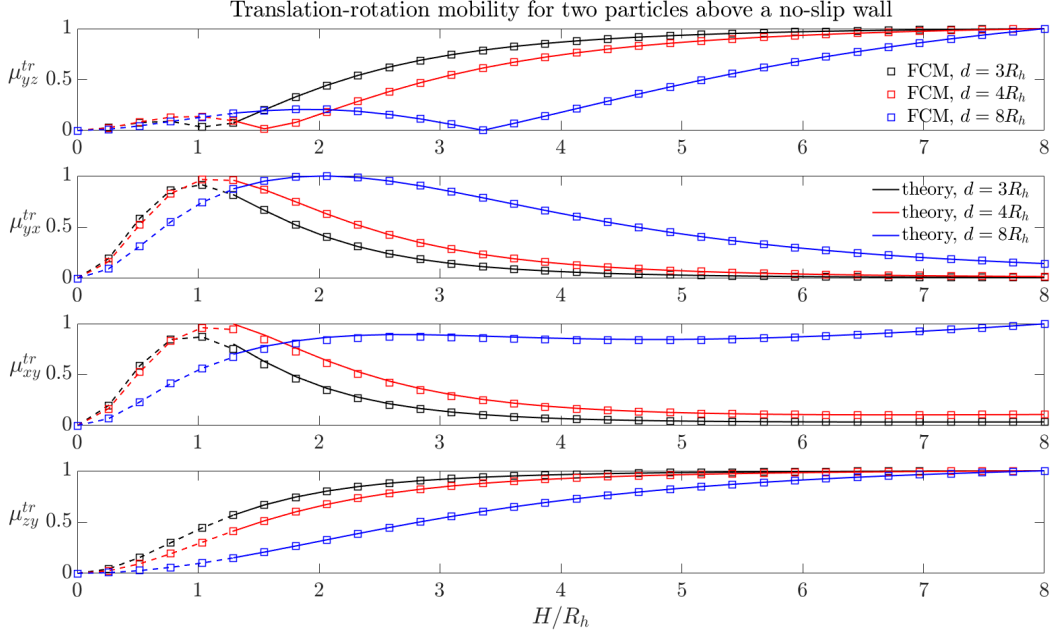


Figure 6: The influence on the linear velocity of q_2 given a unit torque on q_1 . The solid lines correspond to the direct formulas of Swan and Brady. The open square markers are the results from our simulation, using 200 points in each direction. For each distance, both the theory and numerical results are normalized by the maximum value obtained by the numerics. We are in reasonable agreement with the theoretical predictions.

The following figure illustrates the effect of adding or subtracting the image of the dipole kernel near the wall on the translation-rotation pair-mobility.

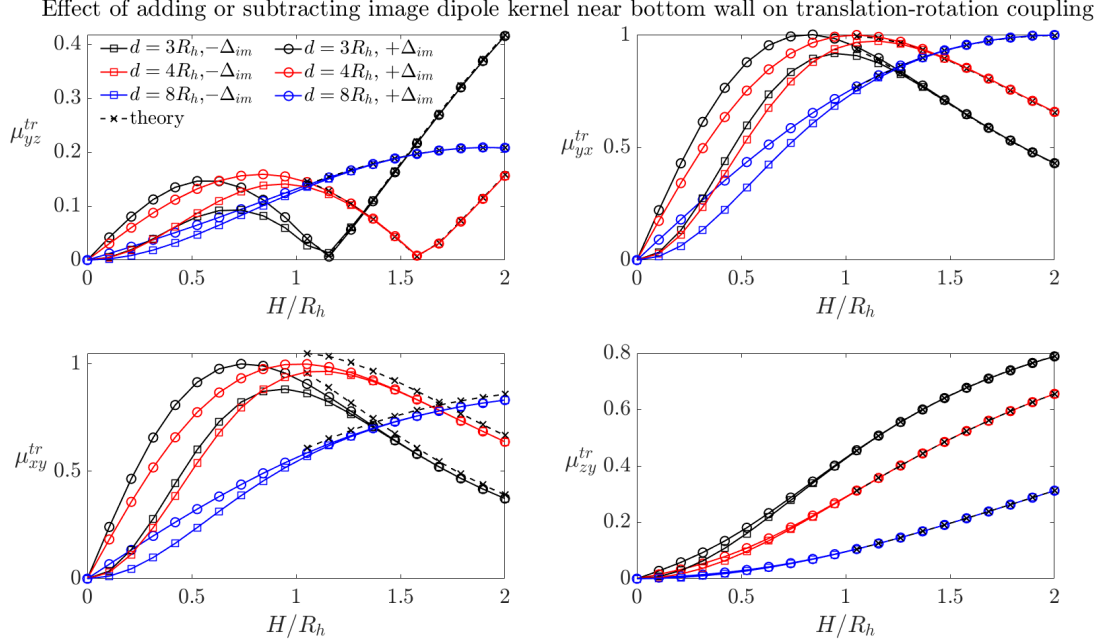


Figure 7: The influence on the linear velocity of q_2 given a unit torque on q_1 . Circle markers result from adding the image of the dipole kernel near the wall, while square markers correspond to subtraction. Both the theory and numerical results are normalized by the same factors used in the previous figure.

4.3.3 Rotational-Rotational coupling

We use the same setup as in the previous section, except we measure the angular velocity of q_2 .

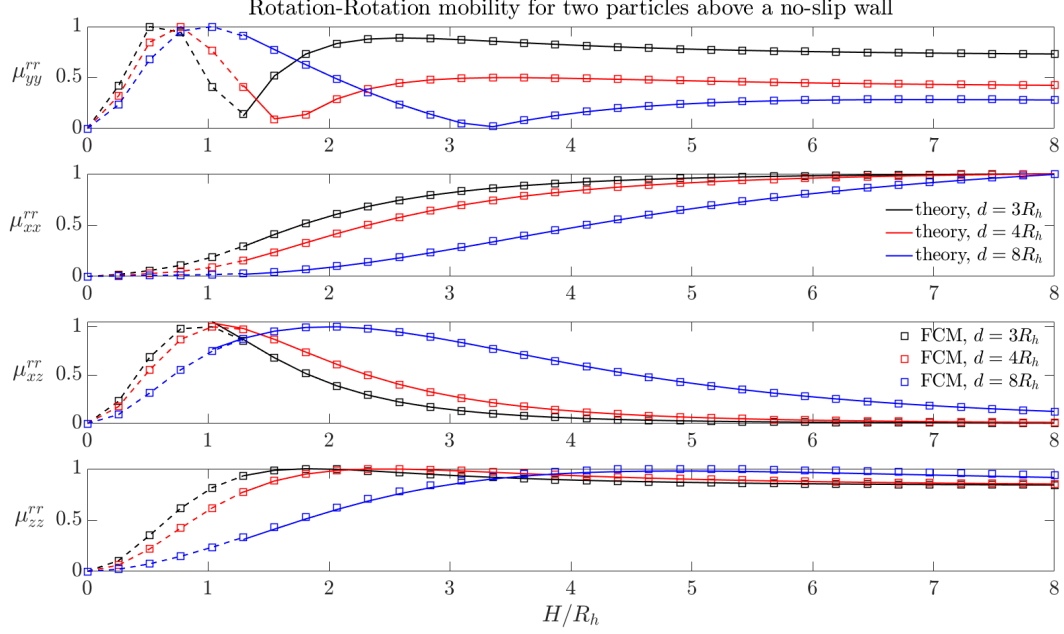


Figure 8: The induced angular velocity of q_2 given a unit torque on q_1 . The solid lines correspond to the direct formulas of Swan and Brady. The open square markers are the results from our simulation. We are in reasonable agreement with the theoretical predictions. We used 200 points in each direction. For each distance, both the theory and numerical results are normalized by the maximum value obtained by the numerics.

Figure 9 illustrates the effect of adding or subtracting the image of the dipole kernel near the wall on the rotation-rotation pair-mobility.

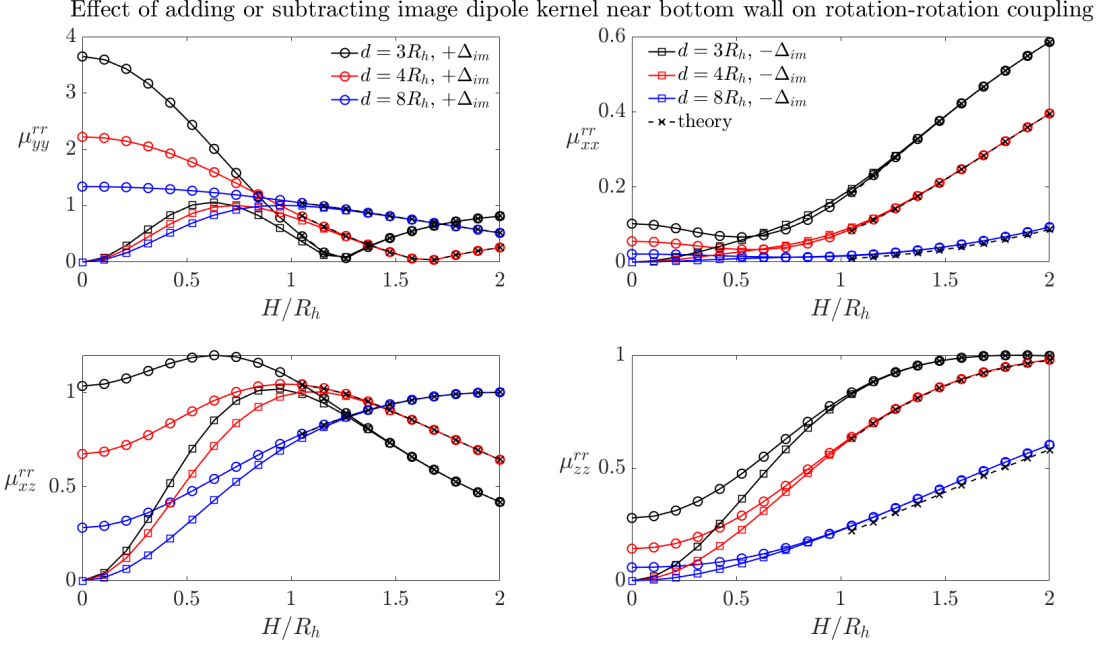


Figure 9: The induced angular velocity of q_2 given a unit torque on q_1 . Circle markers result from adding the image of the dipole kernel near the wall, while square markers correspond to subtraction. Both the theory and numerical results are normalized by the same factors used in the previous figure.

4.4 Positive definiteness of the mobility matrix \mathcal{M} for the bottom wall geometry

Here, we confirm that our solver maintains symmetry and positive definiteness of the mobility matrix \mathcal{M} in Eq. 4.4 by examining, over several trials, the minimum eigenvalues of \mathcal{M} , as well as its relative asymmetry, given by $\|\mathcal{M} - \mathcal{M}^T\|/\|\mathcal{M}\|$. The domain in x, y and z is $L = 10$, with 64 points in each direction. We randomly and uniformly select position pairs of particles of size $R_h = 1$ throughout the domain with at least $4g_w$ separation from the open wall. The columns of \mathcal{M} are the linear and angular velocities of q_1 and q_2 when the force and torque are defined by the corresponding column of the 12×12 identity matrix. The results for 50 randomly positioned particle pairs are shown in Figure 10.

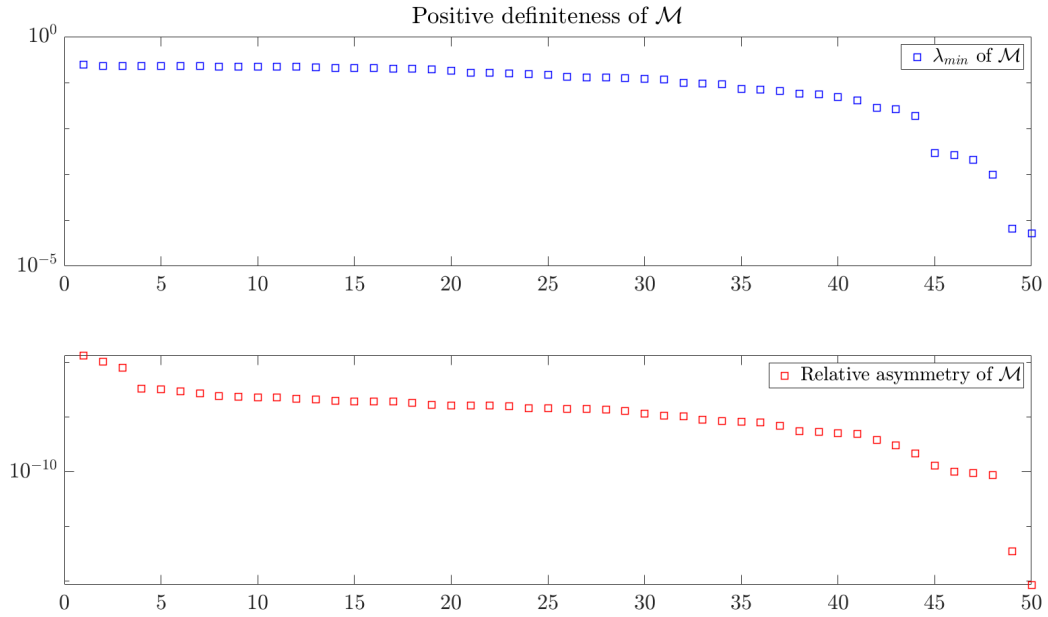


Figure 10: We see that symmetry is well maintained, with all asymmetries less than 10^{-7} and most between 10^{-8} and 10^{-10} . Furthermore, all eigenvalues of the symmetrized mobility matrix are greater than 10^{-5} .

5 Replacing the Gaussian kernel

In order to reduce the costs associated with spreading the forces to the grid and interpolating velocities, we consider replacing the Gaussian kernels given in Eqs. 1.4 - 1.5 with a new kernel introduced in [6]. This “exponential of a semicircle” (ES) kernel is given by

$$\phi_\beta(z; \alpha) = \frac{1}{\int_{-\alpha}^{\alpha} e^{\beta(\sqrt{1-(\frac{z}{\alpha})^2}-1)} dz} \begin{cases} e^{\beta(\sqrt{1-(\frac{z}{\alpha})^2}-1)}, & |\frac{z}{\alpha}| \leq 1 \\ 0, & \text{otherwise.} \end{cases} \quad (5.1)$$

Here, $\alpha = wh/2$, where h is the grid spacing in x and y , w is the number of points to which we spread in each direction, and we’ve normalized the kernel so that integrating it over its support gives 1. Our goal is to determine the smallest $w \in \{4, 5, 6\}$ which yields the smallest error with $\beta \in [1, 3]w$, measured relative to results with the Gaussian kernels and accounting for loss of translational invariance. Ideally, we can use $w \leq 6$ to spread the monopole and dipole kernels.

5.1 Effective hydrodynamic radius formulae for monopole and dipole kernels

First, we need to determine the effective hydrodynamic radius of a particle given w and h and also the relative rescaling in w for the dipole term. For a sphere of radius R_h translating with velocity \mathbf{U} in *unbounded* space, the force exerted by the sphere on the fluid is

$$\mathbf{F} = 6\pi\eta R_h \mathbf{U}. \quad (5.2)$$

A sphere rotating with angular velocity $\boldsymbol{\Omega}$ in unbounded space exerts the torque

$$\mathbf{T} = 8\pi\eta R_h^3 \boldsymbol{\Omega}. \quad (5.3)$$

These are Stokes’ Law and its rotational analog, respectively. In the case of a *triply periodic* domain with a cubic unit cell of length L , Hasimoto computes explicitly in [7] the periodic correction to Stokes’ Law in terms of an asymptotic expansion in R_h/L . To leading order, the expansions for \mathbf{F} and \mathbf{T} which are valid in the *doubly periodic* domain are

$$\mathbf{F} = \frac{6\pi\eta R_h \mathbf{U}}{1 - C_f \left(\frac{R_h}{L} \right)}, \quad (5.4)$$

$$\mathbf{T} = \frac{8\pi\eta R_h^3 \boldsymbol{\Omega}}{1 - C_\tau \left(\frac{R_h}{L} \right)^3}, \quad (5.5)$$

where C_f and C_τ are constants independent of R_h and L . Equipped with Eqs. 5.2 - 5.5, we have a strategy to determine the effective radii for the monopole and relative rescaling for the dipole involving an extrapolation step with Eqs. 5.2 - 5.3, followed by routine calculations with Eqs 5.4 - 5.5.

- (Extrapolation) If we fix the position of the particle and support α of the spreading kernel, Eq. 5.2 tells us that the translational mobility given a unit force should approach the free mobility for a given hydrodynamic radius, i.e. $1/(6\pi\eta R_h)$, as $L_{xy} \rightarrow \infty$. In other words, the normalized mobility should approach 1. Similarly, Eq. 5.3 says that the rotational mobility should approach $1/(8\pi\eta R_h^3)$ as $L_{xy}^3 \rightarrow \infty$. As a sanity check, Figure 11 ensures this is the case for the Gaussian kernel where the force is in the parallel direction and torque is about the z -axis.

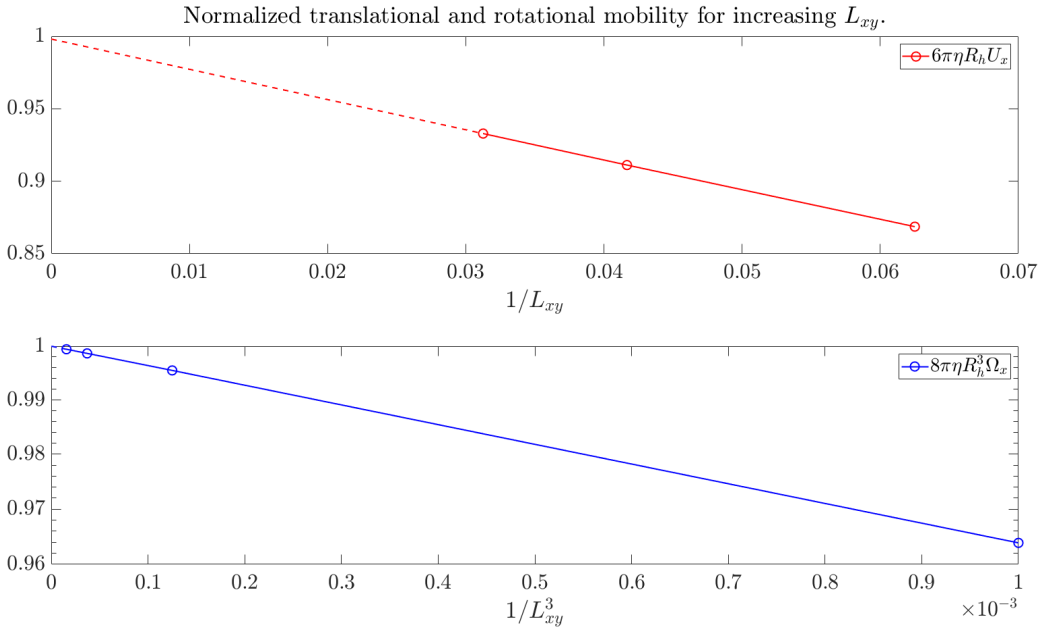


Figure 11: Extrapolating translational and rotational mobility for the Gaussian kernel as $L_{xy} \rightarrow \infty$ for the doubly periodic (no-wall) geometry. The top panel used $R_h = 1$, and the bottom uses $R_h = 4$. Note that we set the $k = 0$ mode of forces on the grid to 0 in order to ensure the total force on the system is 0. We don't do this for the dipole. The extrapolated intercepts are close enough to 1 to pass our sanity check. The Chebyshev grid ran from -10 to 10 , and we chose $N_{xy} = N_x$ such that h_{xy} was the same for each L_{xy} .

For the ES kernel, we can use the same approach in the doubly-periodic (no wall) geometry to determine the function $c(w)$ such that

$$R_h(w; h_{xy}) = h_{xy}c(w). \quad (5.6)$$

Observe that inserting this into Eq. 5.2, assuming $\mathbf{F} = (1 \ 0 \ 0)^T$ and taking $L_{xy} \rightarrow \infty$ gives

$$c_f(w) = \frac{1}{6\pi\eta h_{xy}U_x(w)}, \quad (5.7)$$

where we've included in U_x a dependence on w . Similarly, if we insert Eq. 5.6 into Eq. 5.3 and assume $\mathbf{T} = (0 \ 0 \ 1)^T$, we have

$$c_\tau(w) = \sqrt[3]{\frac{1}{8\pi\eta h_{xy}^3\Omega_z(w)}}. \quad (5.8)$$

So, if we keep α fixed for some $w \in \{4, 6, 8, 10\}$ as L_{xy} is increased, we can extrapolate from the values of $U_x(w_f; L_{xy})$ and $\Omega_z(w; L_{xy})$ resulting from a unit force in the x direction and torque about the z -axis, respectively, to determine $U_x(w), \Omega_z(w)$ and the dimensionless radii $c_f(w), c_\tau(w)$. **We only need to do this for one w and β .**

- Now that we have $c_f(w)$ and $c_\tau(w)$ for a single width, we can use Eqs. 5.4 - 5.5 to determine the constants C_f and C_τ . Then, we only need a single mobility test at other combinations of w and β to determine R_h for the monopole and dipole, without relying on extrapolation. **These should give correct normalized mobilities in the bottom-wall, two-wall and triply periodic cases as well.**

In Figure 12, we perform the extrapolation and compute radii fits for 30 particle positions distributed uniformly in a cube of width h_{xy} at the center of the grid and for several widths and β s. We also compare radii extrapolated from our triply periodic FCM code for the monopole.

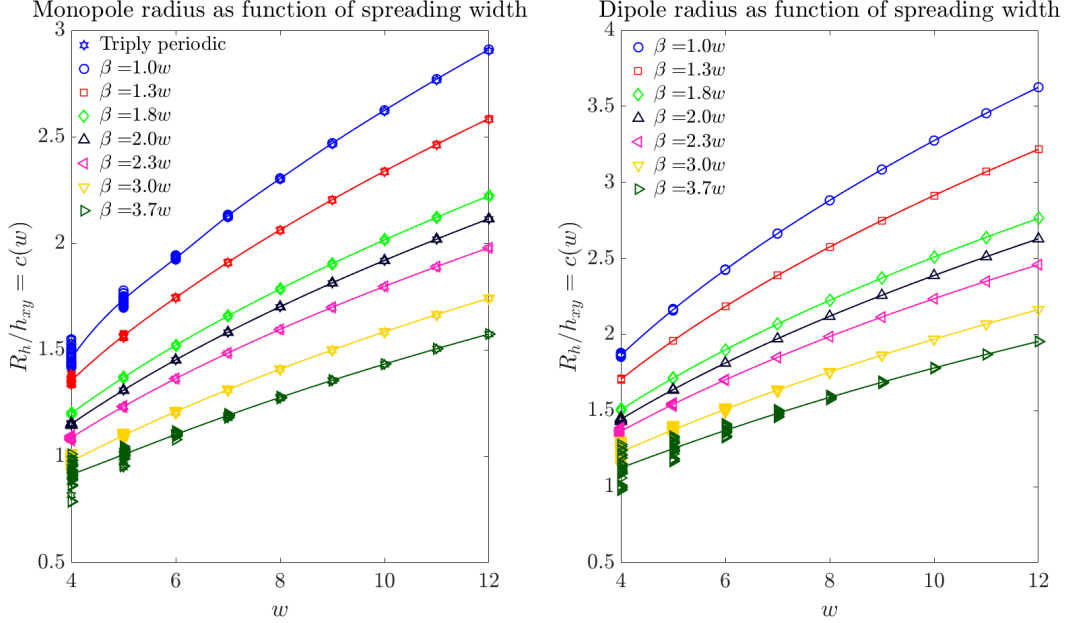


Figure 12: Hydrodynamic radius fits for the monopole and dipole kernels for several β . The star markers (for monopole only) correspond to extrapolations computed using the triply periodic FCM solver, as opposed to our doubly periodic one (all other markers). The lines pass through the averages over the spread in radii at each width of the doubly periodic data. We see that the radii computed by both solvers are in good agreement, differing slightly only after the first 3 significant digits. As was the case for the Gaussian kernel, the width of the dipole is smaller than that of the monopole given a fixed radius. The Chebyshev grid ran from -10 to 10 , and we chose N_{xy} such that $h_{xy} = 0.3125$ was the same for each L_{xy} used to extrapolate.

The spreads in radii at a given w indicate the degree to which we lose translational invariance given our choice of β . Clearly, **for a given width, there is an optimal β which yields the smallest spread in effective radius**. In Fig. 13, we evaluate percent errors in the extrapolated radii at each w and for each β in terms of a 95% confidence interval. That is, we report

$$\%-\text{error} = \frac{4\sigma(w)}{\overline{R}_h(w)} \times 100\%,$$

in which $\sigma(w)$ is the standard deviation from the mean radius $\overline{R}_h(w)$.

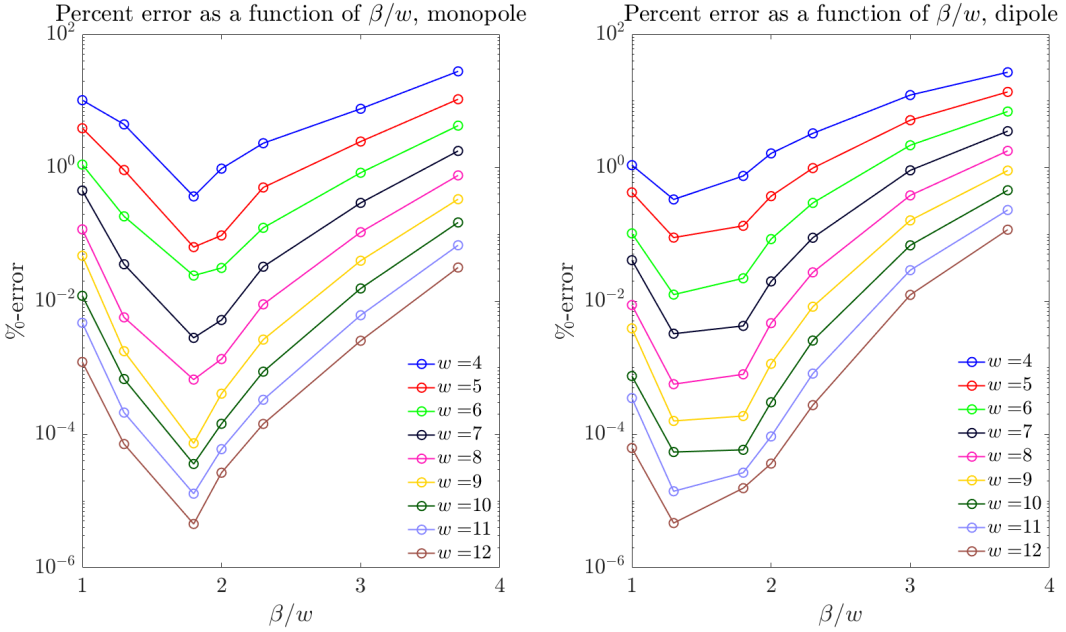


Figure 13: Percent errors as a function of β for $w = 4, 5, \dots, 12$ for both the monopole and dipole kernels.

Now that we have an idea of how the errors behave as β and w vary, we turn to further probing this behavior for a subset of w and β for the monopole and dipole. Specifically, we consider $w = 4, 5, 6$ and $\beta/w \in [1.2, 2.3]$ for the monopole, or $\beta/w \in [1.0, 2.3]$ for the dipole. These β/w intervals are chosen differently for the monopole and dipole to correspond with the optimal error basins for each given the viable widths, which should be clear from Figure 13. The radii for the subset of widths and refined β/w intervals are shown in Figure 14, and the percent errors are in Figure 15.

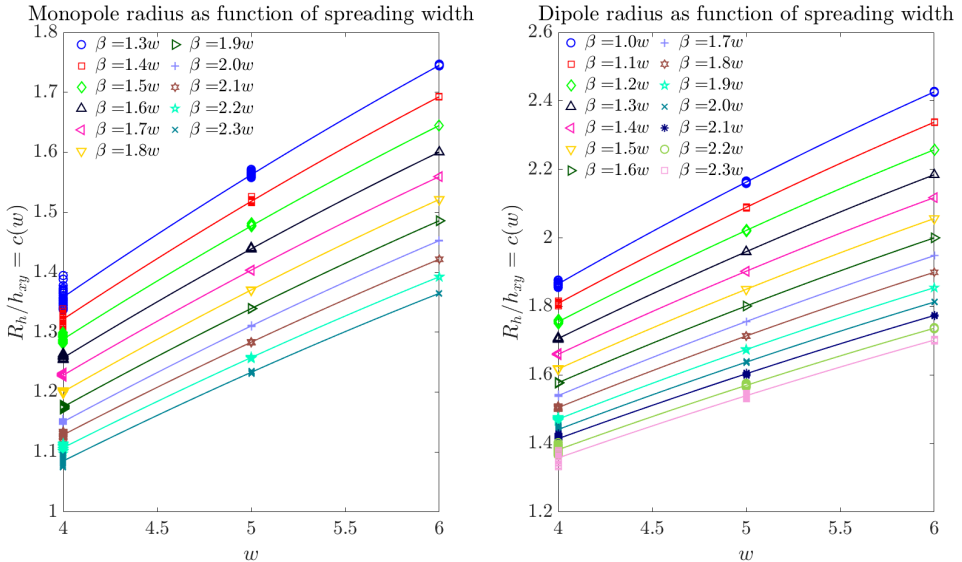


Figure 14: Hydrodynamic radius fits for the monopole and dipole kernels for $w = 4, 5, 6$ and β corresponding to the optimal error basins from Fig. 13. The lines pass through the averages over the spread in radii at each width of the doubly periodic data. The Chebyshev grid ran from -10 to 10 , and we chose N_{xy} such that $h_{xy} = 0.3125$ was the same for each L_{xy} used to extrapolate.

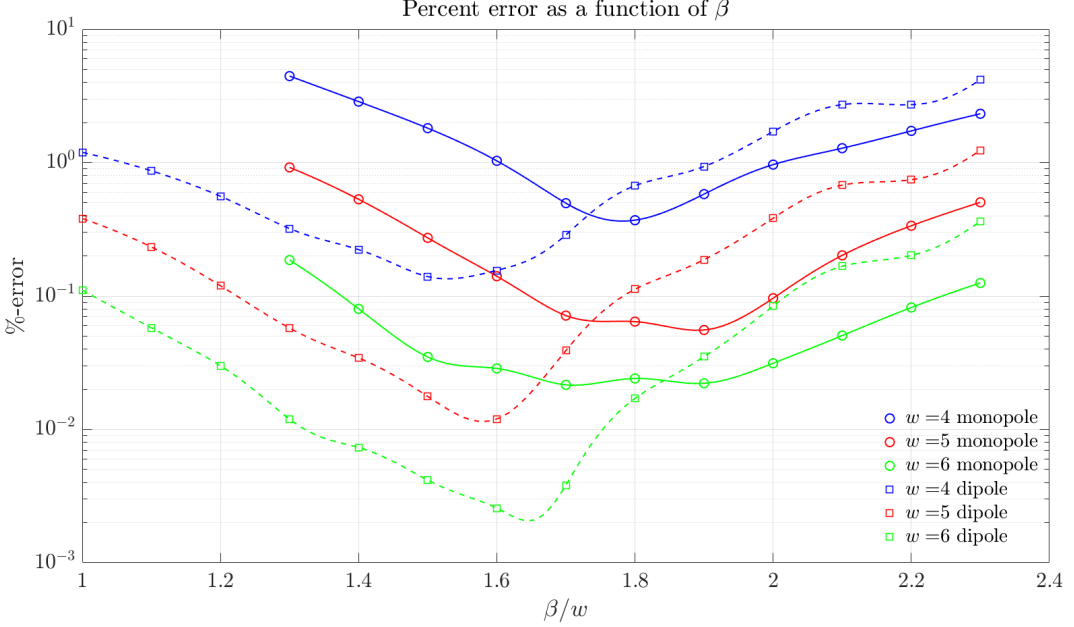


Figure 15: Percent errors as a function of optimal β for $w = 4, 5, 6$ for both the monopole (solid lines) and dipole (dotted lines) kernels.

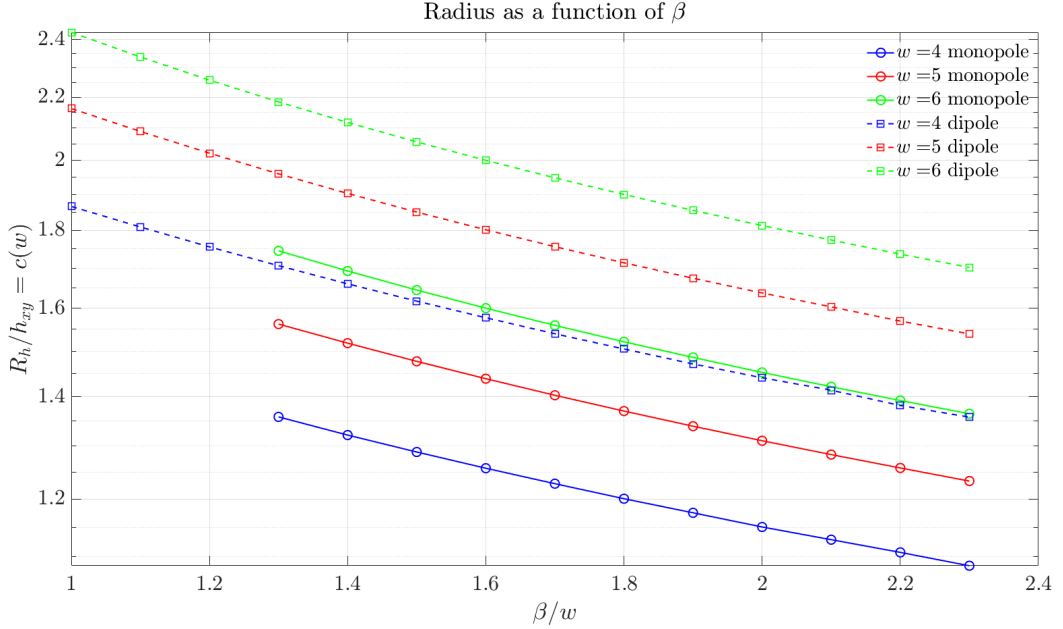


Figure 16: Effective radii as a function of β for $w = 4, 5, 6$ for both the monopole (solid lines) and dipole (dotted lines) kernels.

We see that for all w and β/w , the error will be less than $\sim 4.5\%$ in both the monopole and dipole radii. Taking this as the least tolerable error, Figure 16 makes clear that the options we have for setting β and w for the monopole and dipole kernels are rather constrained. Let β_f denote the setting for the monopole and β_τ for the dipole. There is no way to match the radii except for the settings tabulated in Table 1, which also shows the min and max errors obtained for each setting.

Table 1: Possible combinations of w_f , w_τ , β_f and β_τ along with error ranges

w_f	5	6	6	6
w_τ	4	4	5	6
β_f/w_f	[1.3, 1.595]	[1.3, 2.03]	[1.3, 1.515]	[1.3, 1.38]
β_τ/w_τ	$1.154 \frac{\beta_f}{w_f} + 0.1532$	$1.057 \frac{\beta_f}{w_f} - 0.1505$	$1.271 \frac{\beta_f}{w_f} + 0.7298$	$1.505 \frac{\beta_f}{w_f} + 0.2197$
%-error f	< 0.922, > 0.146	< 0.186, > 0.0215	< 0.186, > 0.0338	< 0.186, > 0.096
%-error τ	> 0.236, < 1.611	> 0.1288, < 1.616	> 0.0586, < 0.371	> 0.191, < 0.352

The rescalings between β_τ/w_τ and β_f/w_f were determined by a simple fitting procedure using the data from [Figure 16](#). For cases when we want to use minimal spreading width and only the monopole term, like for rigid multiblobs, we tabulate the errors for viable β_f and $w_f = 4$ in [Table 2](#) which are equivalently shown in [Figure 15](#).

Table 2: Error for each β_f given $w_f = 4$

β_f/w_f	1.3	1.4	1.5	1.6	1.7	1.8	1.9	2.0	2.1	2.2	2.3
%-error f	4.45	2.86	1.81	1.03	0.49	0.37	0.58	0.96	1.28	1.73	2.32

Now, for cases with both the monopole and dipole, we need only confer with [Table 1](#) and pick the combinations of w_τ, w_f, β_τ and β_f that result in a tolerable error. In [Table 3](#), we report the **optimal** combinations of these parameters in the sense of **minimizing the combined error** between the monopole and dipole. Note, the number of digits reported here should be taken with a grain of salt, since we fit splines to the %-errors as a function of β_f and β_τ in order to pin down the optimal combinations.

Table 3: Optimal combinations of w_f , w_τ , β_f and β_τ along with the optimal errors and effective radii

w_f	5	5	6	6	6
w_τ	4	5	4	5	6
β_f/w_f	1.3536	1.3055	1.5728	1.3261	1.3267
β_τ/w_τ	1.7147	2.2320	1.5115	1.7584	2.2160
%-error f	0.6967	0.8968	0.0294	0.1518	0.1511
%-error τ	0.3660	0.8103	0.1281	0.0890	0.2124
R_h/h_{xy}	1.5382	1.5598	1.6121	1.7309	1.7305

In [Figure 17](#), we plot the optimal ES kernels using the settings in [Table 3](#). The grid spacing is 1, and $x \in [-3, 3]$. The solid lines correspond to evaluating the kernel on a refined grid, and the kernel is centered at $x = -0.01$.

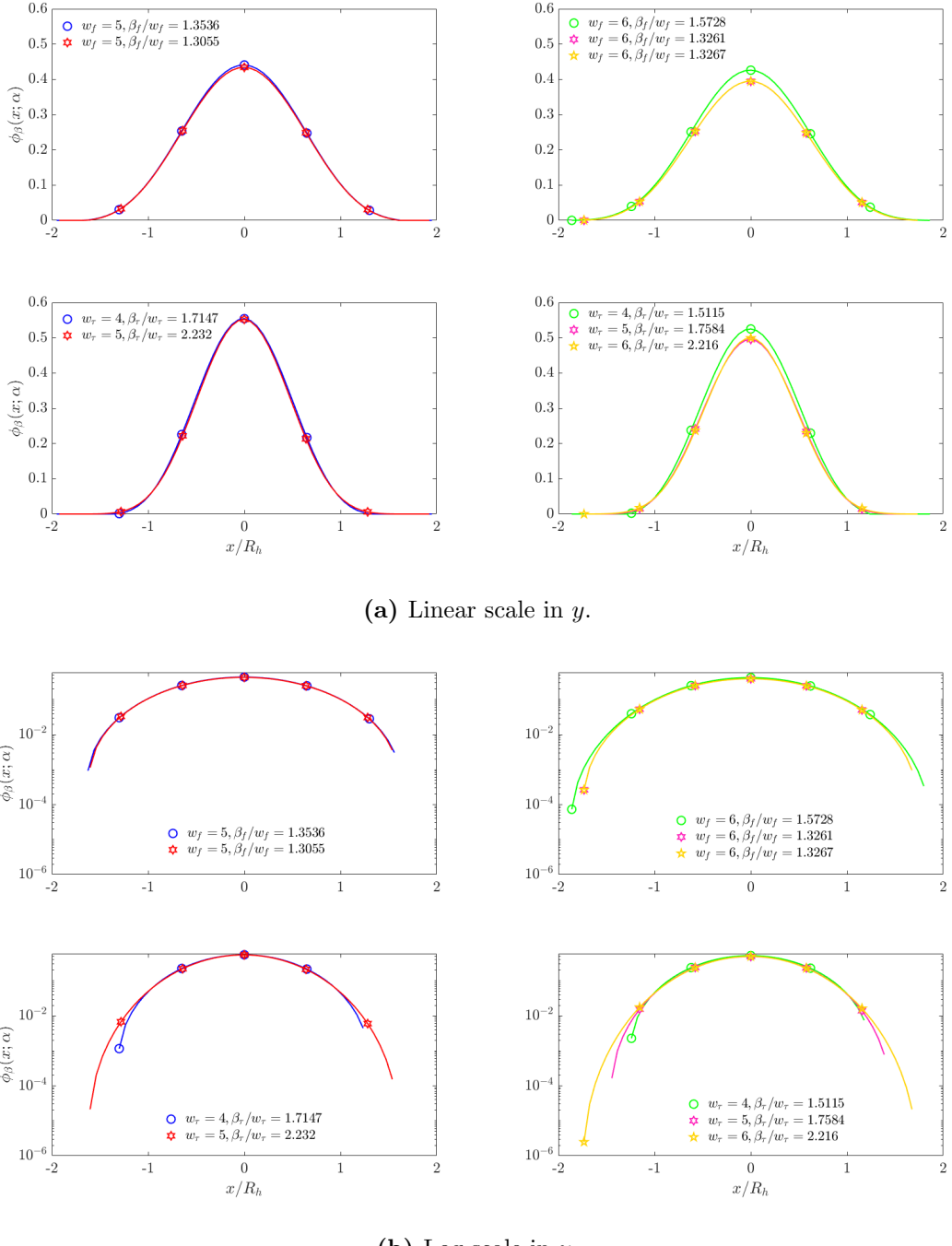


Figure 17: ES monopole and dipole kernels with settings from [Table 3](#).

6 Oscillations in trans-rot mobility near the open boundary

While computing trans-rot mobilities for the ES kernel in the bottom-wall geometry, we noticed oscillations developing as the particle approached the artificial/open boundary. This was most pronounced when the number of Chebyshev points was set according to Eq. 6.1;

$$N_z = \left\lceil \frac{\pi}{\cos^{-1}(-\frac{h_{xy}}{H}) - \frac{\pi}{2}} \right\rceil, \quad (6.1)$$

so that the spacing at the center of the Chebyshev grid approximately matches that in x and y . The error is shown in Fig. 18, where we see that the oscillations diminish as we add more points to the Chebyshev grid.

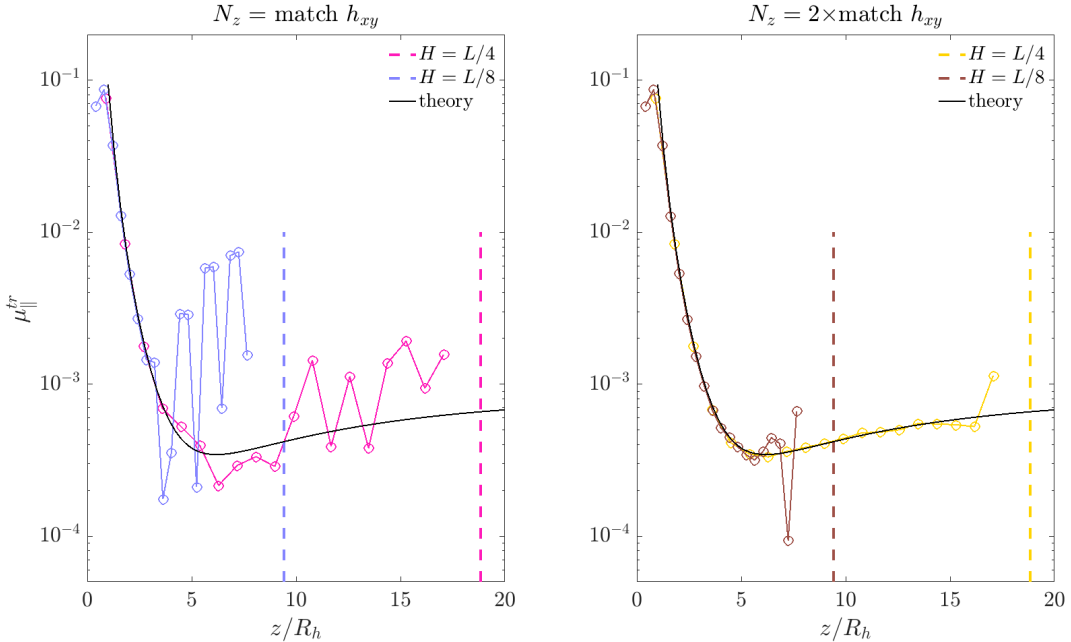


Figure 18: Example of the erroneous oscillations near the open boundary when using the ES kernel, for two positions of the boundary and different spacings in z . Here, $N_{xy} = 128$ and $L = 40$. The black lines correspond to results obtained from the periodized RPY kernel with bottom wall corrections.

At this point, we can imagine several sources for this problem, and a few hints are revealed in Figure 19. Namely, we see that the oscillations are less pronounced in the rot-trans self coupling. The only difference between computing trans-rot and rot-trans is that, in the former, we spread the torque, take its curl spectrally, solve for linear velocity and interpolate; while in the latter, we spread the force, solve for linear velocity, take its curl and interpolate.

This indicates that there may be some issues with the spectral curl of the torques on the grid. When we only spread a force, the RHS of Eqs. 1.23 - 1.24 are smooth, requiring only one derivative in z . Since our BVP solver is also a smoother, when we take the curl of the linear velocities, it's possible that the smoothness gained through the BVP solve mitigates loss in smoothness when computing the curl. On the other hand, when we spread only a torque and take its curl, the RHS of Eqs. 1.1 is not as smooth, and even less-so for Eqs. 1.23 - 1.24 since we must further differentiate in z .

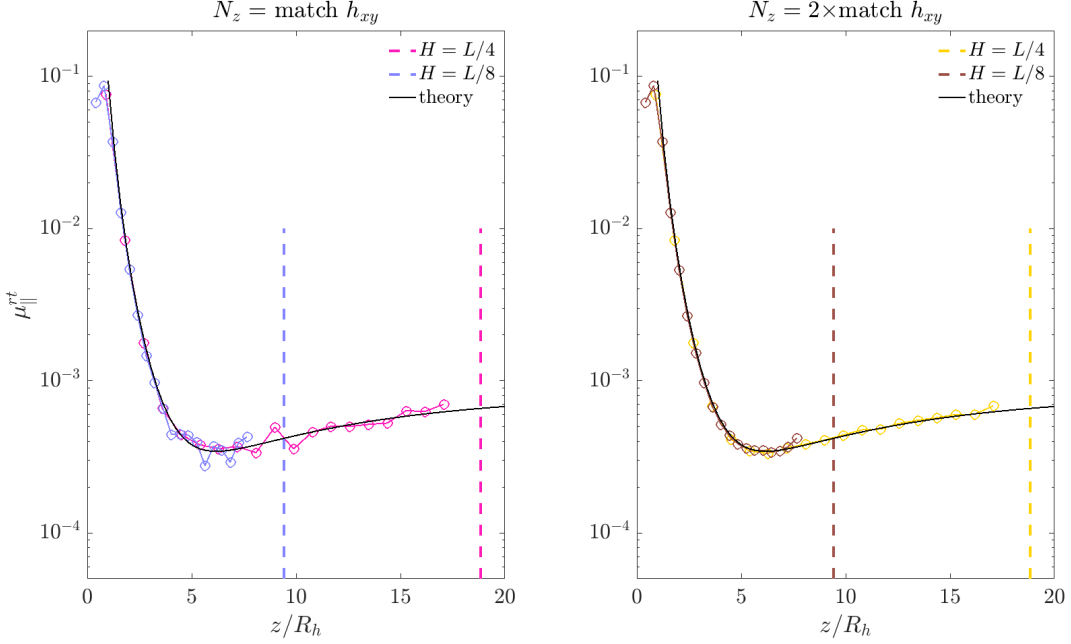


Figure 19: The setup is the same as in Fig. 18, except we compute **rot-trans self coupling**.

In this case, it may be that the BVP solve does not smooth the linear velocities enough, which is problematic if there are high-frequency Fourier spectra in the RHS of Eqs. 1.23 - 1.24 when we're near the open boundary (it turns out that the high degree Chebyshev coefficients are the issue).

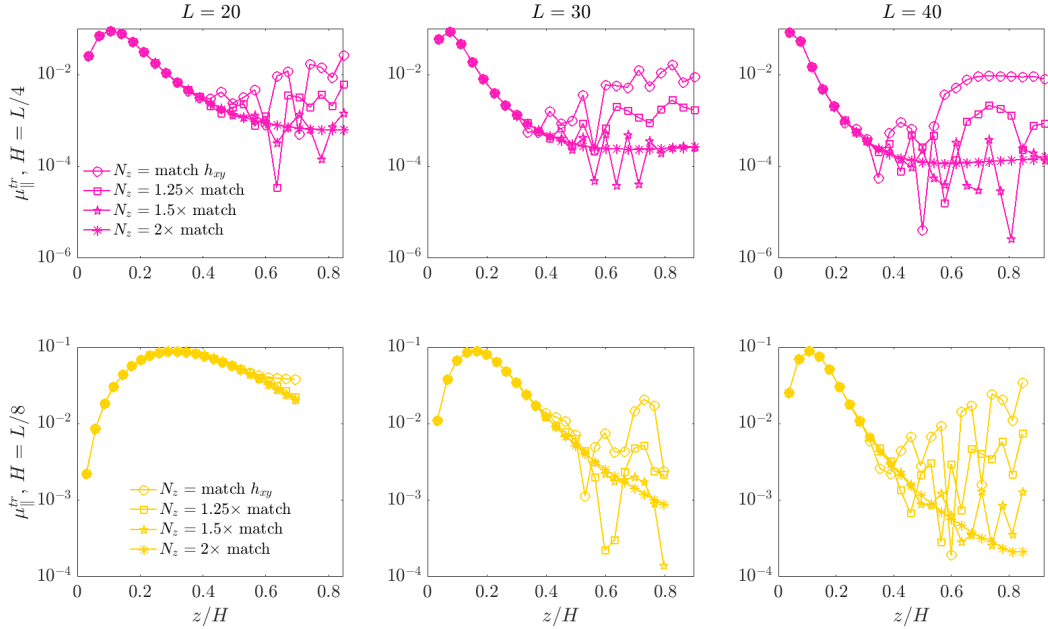


Figure 20: Example of the erroneous oscillations near the open boundary when using the Gaussian kernel, for two positions of the boundary, three lengths and different spacings in z . Here, h_{xy} is the same in each plot, and so is R_h . The x-axis represents fractional location in the domain, measured from the bottom wall.

It will be easier to get a handle on the oscillatory behavior by examining if it persists for an untruncated Gaussian. In Figures 20 - 21, we investigate the oscillations near the open boundary when using the Gaussian kernel without truncation and compare using the spectral and analytical curls of the dipole Gaussian. Note, instead of plotting the mobilities as a function of relative particle height, we plot them against the fractional location of the particle in the domain, measured from the bottom wall. From Fig. 20, we see that the oscillations generally begin for N_z matching h_{xy} when $z \geq 0.3H$, independent of L . As before, they diminish as points are added to the Chebyshev grid.

Figure 21, which shows the results from using the analytical curl of the dipole Gaussian, seems to improve on things significantly. We only need to multiply the number of Chebyshev points from Eq. 6.1 by 1.25 to reduce most of the oscillations. By “use the analytical curl”, we mean that all partial derivatives in Eq. 6.2 are spread onto the grid directly with the analytical derivatives of the kernel;

$$\text{RHS of Eq. 1.1} = \mathbf{S}_f \mathcal{F} + \frac{1}{2} \nabla \times (\mathbf{S}_\tau \mathcal{T}) = \frac{1}{2} \begin{pmatrix} \partial_z \mathcal{T}^y - \partial_y \mathcal{T}^z \\ \partial_x \mathcal{T}^z - \partial_z \mathcal{T}^x \\ \partial_x \mathcal{T}^y - \partial_y \mathcal{T}^x \end{pmatrix} - \begin{pmatrix} \mathcal{F}^x \\ \mathcal{F}^y \\ \mathcal{F}^z \end{pmatrix}. \quad (6.2)$$

Note, this is instead of the spectral evaluation given in Eq. 3.1. More specifically, we have

$$\nabla \times (\mathbf{S}_\tau(\mathbf{x}) \mathcal{T}) = \sum_{k=1}^M \begin{pmatrix} \tau_z(\mathbf{y}_k) \partial_y - \tau_y(\mathbf{y}_k) \partial_z \\ \tau_x(\mathbf{y}_k) \partial_z - \tau_z(\mathbf{y}_k) \partial_x \\ \tau_y(\mathbf{y}_k) \partial_x - \tau_x(\mathbf{y}_k) \partial_y \end{pmatrix} \Delta_\tau(\mathbf{x} - \mathbf{y}_k) \quad (6.3)$$

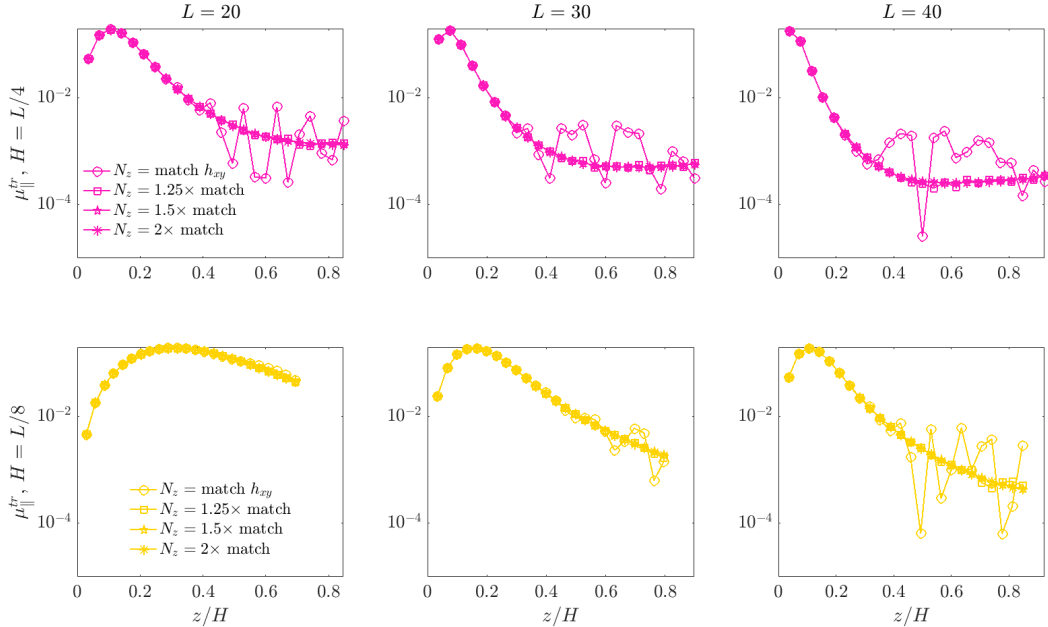


Figure 21: The setup is the same as in Fig. 20, except we **spread the analytical curl** of the Gaussian

6.1 Spreading torque using the derivative of the ES kernel with $w_f = w_\tau = 6$

Here, we confirm that using the analytical curl of the ES dipole kernel gives reasonable trans-trans, rot-rot, rot-trans and trans-rot mobilities. For trans-rot, we know that matching the spacing at the middle of the Chebyshev grid to h_{xy} still results in an under-resolved mobility. So, we consider several aspect ratios, periodic lengths and positions of the open boundary to determine by how much we need to increase N_z to get reasonable results. The derivative of the kernel is given by

$$\phi'_\beta(z; \alpha) = \frac{-\beta z \phi_\beta(z; \alpha)}{\alpha^2 \sqrt{1 - (\frac{z}{\alpha})^2}}. \quad (6.4)$$

While the derivative is singular for $|z/\alpha| = 1$, there are local optima around this point. By solving for the location of these optima, we find a new point of truncation;

$$z_{\text{trunc}}(\alpha, \beta) = \frac{\alpha \left(\frac{6((8\beta^2 + 12\sqrt{-12\beta^2 + 81} - 108)\beta)}{\beta} \right)^{1/3} + \frac{24\beta}{\left((8\beta^2 + 12\sqrt{-12\beta^2 + 81} - 108)\beta \right)^{1/3} + 12}}{6}. \quad (6.5)$$

That is, $1 \approx z_{\text{trunc}}/\alpha < 1$, and we set the derivative to 0 for $|z| > z_{\text{trunc}}$.

6.1.1 Trans-rot in bottom wall

For Figures 22 - 24, $h_{xy} = 0.4$ and the reference result is computed on a doubled grid in each direction (with double spreading width). At a given aspect ratio, larger values of `fac` are required as L increases. At a fixed length, smaller values of `fac` in $N_z = \text{fac} \times \text{match}$ h_{xy} are needed as the position of the open boundary position decreases. Noting the oscillations in the reference results for $L = 30, 40$, we see that they arise when the particle reaches a height that gives a local minimum in its mobility. In a half space, the trans-rot self coupling should decay, so we suspect this is related to periodic images.

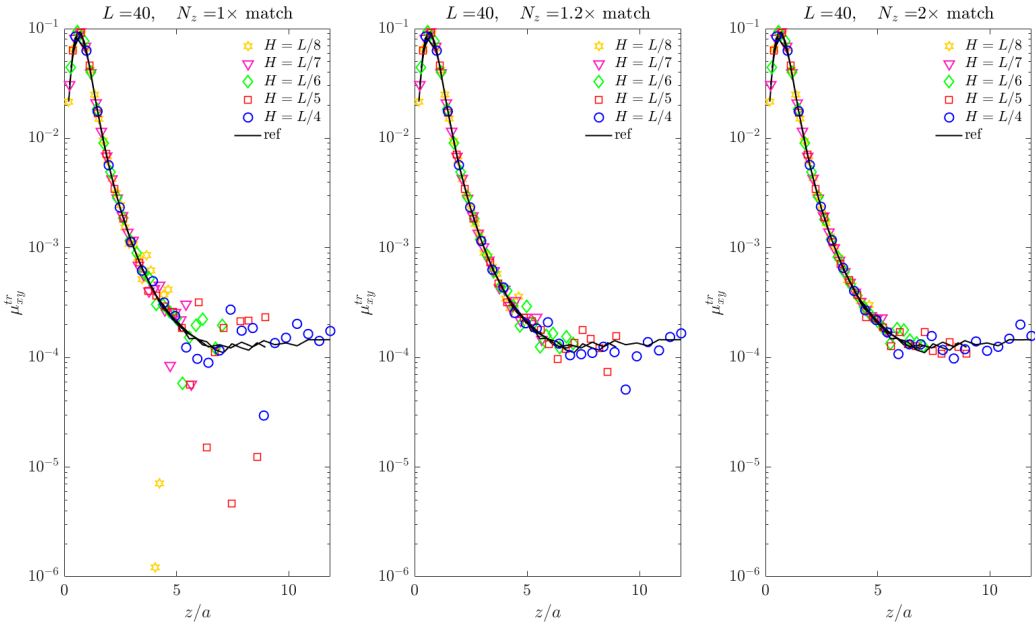


Figure 22: Trans-rot self mobility for $L = 40$ and fixed `fac` as H is increased.

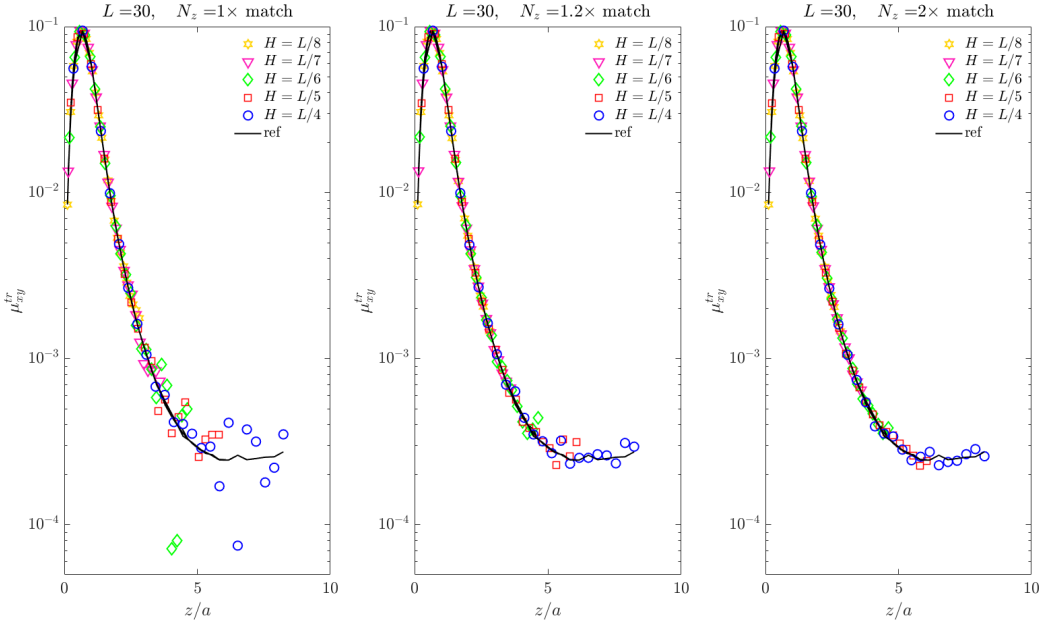


Figure 23: Trans-rot self mobility for $L = 30$ and fixed `fac` as H is increased.

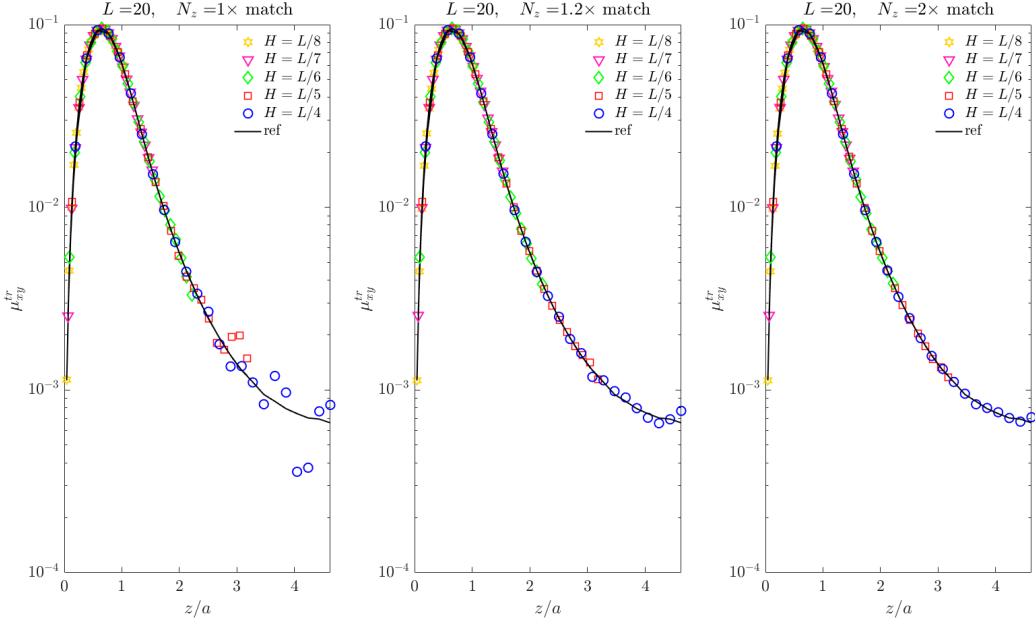


Figure 24: Trans-rot self mobility for $L = 20$ and fixed `fac` as H is increased.

We may be able to better understand how images and numerics contribute to oscillations by considering the analytical form of $\mu_{\parallel}^{tr}(z)$ (from RPY+Wall tensor) for two particles at the same height z in the limit of $R_h \rightarrow 0$. It is given by

$$\mu_{\parallel}^{tr}(z) = \frac{3\hat{r}_z(\hat{r}_x)^2}{\|\mathbf{r}\|^2}, \quad \text{where } \mathbf{r} = \begin{pmatrix} x_1 - x_2 \\ y_1 - y_2 \\ 2z \end{pmatrix}, \quad \hat{\mathbf{r}} = \frac{\mathbf{r}}{\|\mathbf{r}\|}, \quad (6.6)$$

and x_1, y_1, x_2, y_2 are the x and y coordinates of particles one and two. We can approximate the sum of this term over the images with an integral in polar coordinates (done in Maple). We find that as $z \rightarrow \infty$, the approximate sum converges to $\frac{2\pi}{L}$. The self term decays like R_h/z^4 . So, the combined mobility (self+images) is dominated by the self term for small h and by the images for large h . This results in a minimum in $\mu_{\parallel}^{tr}(z)$, followed by a plateau;

$$z_{\min} \sim (L^3 R_h^2)^{1/5}. \quad (6.7)$$

If the particle goes above z_{\min} , the mobility is no longer physically correct. This may explain the oscillations in the reference mobility we observed for $L = 30, 40$.

6.1.2 Rot-trans in bottom wall

In all of the following figures, $h_{xy} = 0.4$ and the reference result is computed on a doubled grid in each direction (with double spreading width). We are checking the rot-trans coupling in the xy -plane, i.e. the resulting angular velocity about the y axis given a unit force in the x direction.

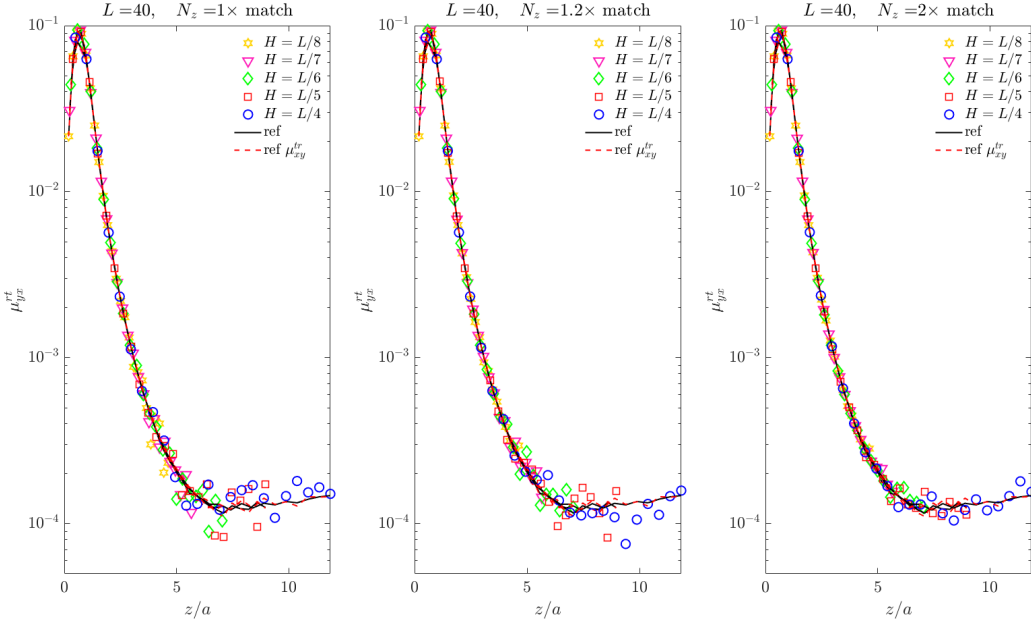


Figure 25: Rot-trans self mobility for $L = 40$ and fixed `fac` as H is increased. The dashed red line is the reference result for μ_{xy}^{tr} .

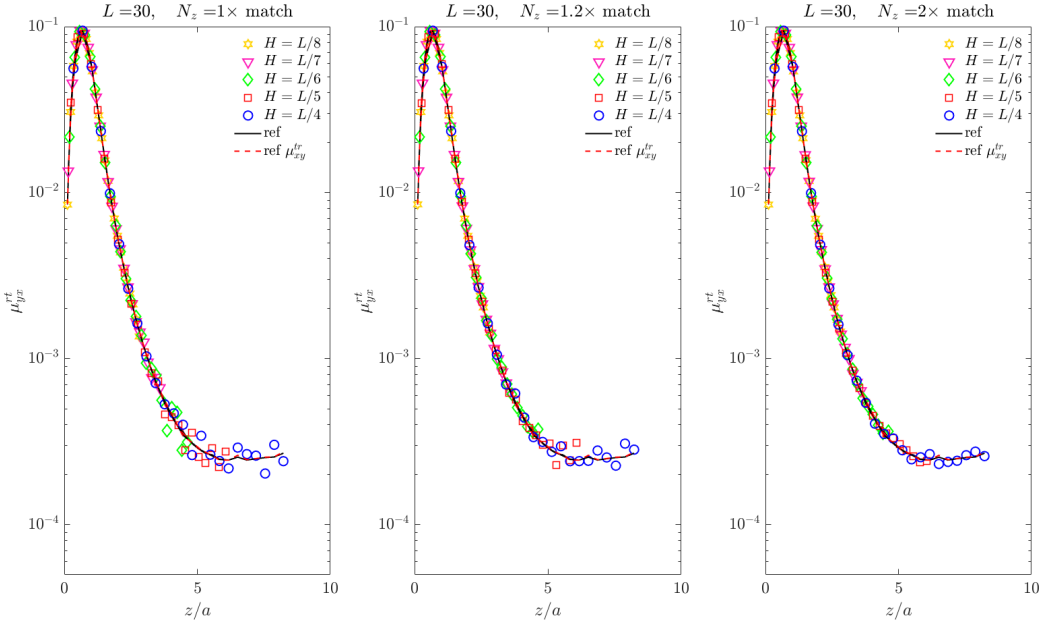


Figure 26: Rot-trans self mobility for $L = 30$ and fixed `fac` as H is increased. The dashed red line is the reference result for μ_{xy}^{tr} .

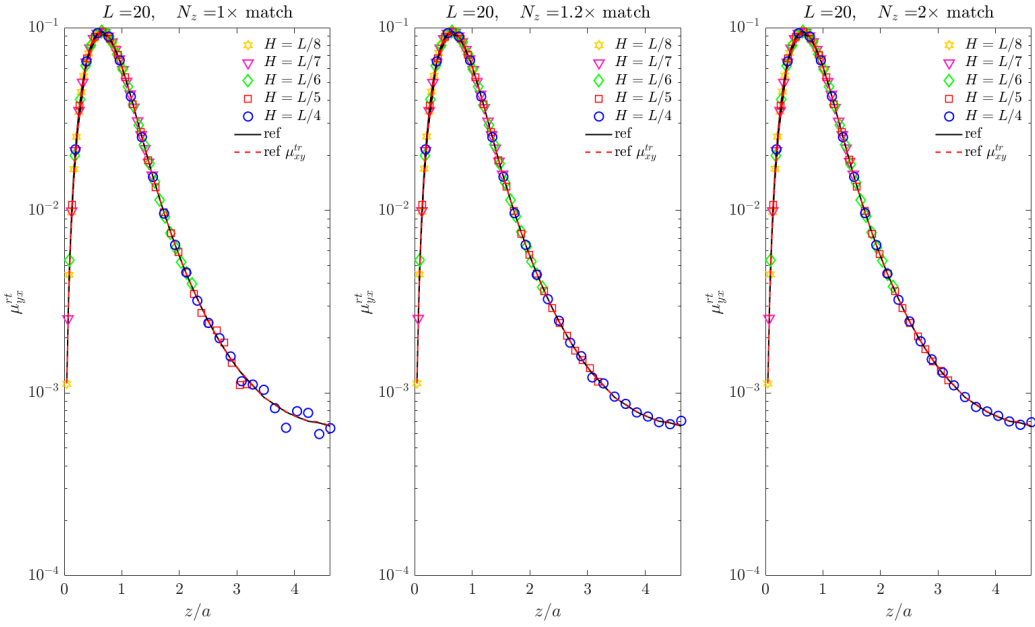


Figure 27: Rot-trans self mobility for $L = 20$ and fixed `fac` as H is increased. The dashed red line is the reference result for μ_{xy}^{tr} .

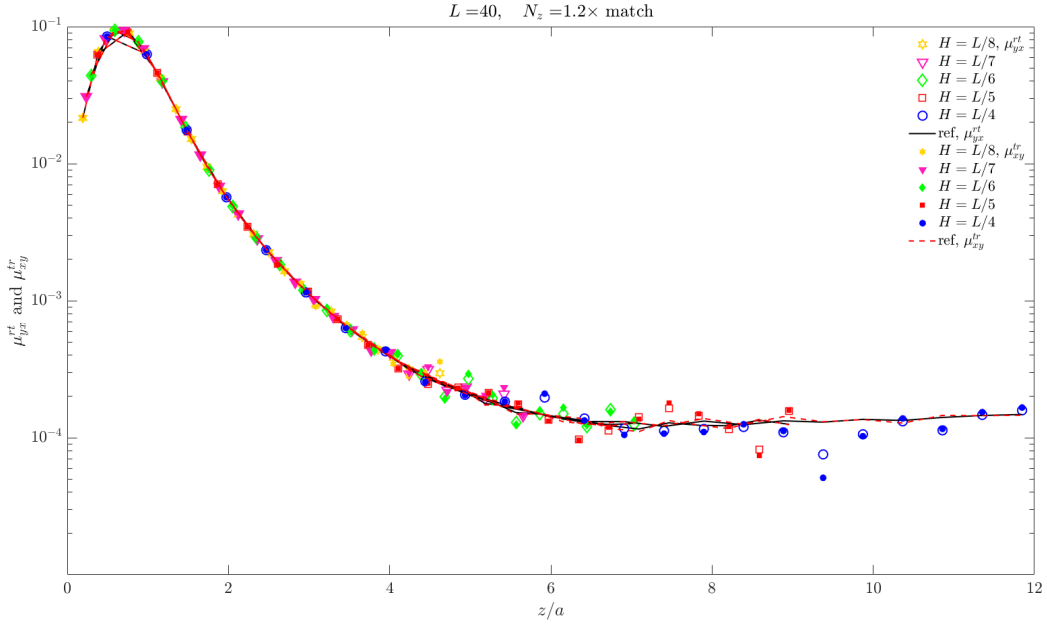


Figure 28: Rot-trans (unfilled) and trans-rot (filled) self mobility for $L = 40$ and fixed `fac` as H is increased. Reference results for rot-trans are the solid black lines, and those for trans-rot are the dashed red lines.

6.1.3 Asymmetry between rot-trans and trans-rot in bottom wall

From the symmetric property of the mobility tensor, we know that rot-trans and trans-rot results should be similar. In Figure 29, we show the absolute asymmetry between the two mobility calculations, given by $|\mu_{yx}^{rt} - \mu_{xy}^{tr}|$.

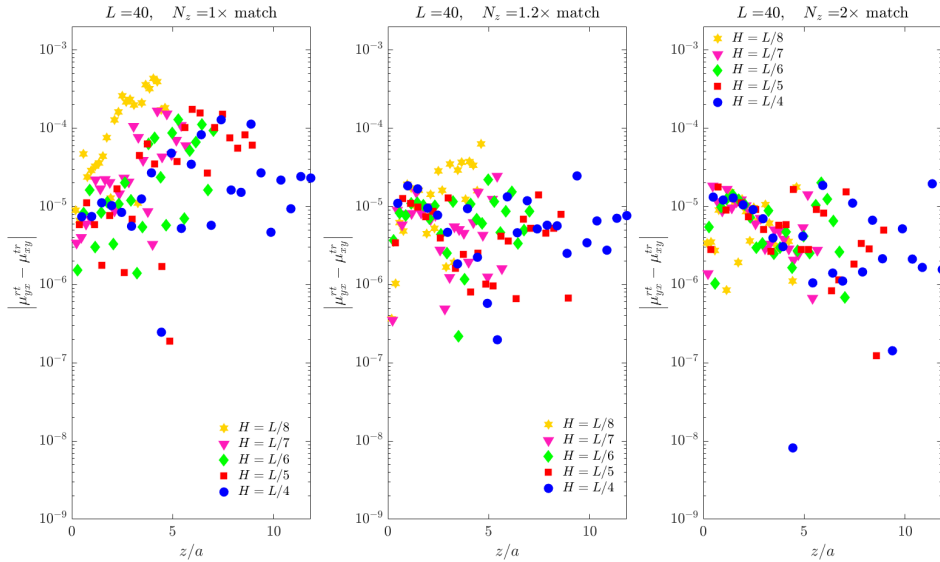


Figure 29: Absolute asymmetry in rot-trans for $L = 40$ and fixed `fac` as H is increased.

6.1.4 Improving symmetry between rot-trans and trans-rot by adjoint interpolation

Altogether, the mobility matrix in Eq. 4.4 has the form

$$\mathcal{M} = \mathcal{J}\mathcal{F}_{xy}^*\mathcal{L}_z^{-1}\mathcal{F}_{xy}\mathcal{S}, \quad (6.8)$$

where \mathcal{L}_z^{-1} represents the independent BVP solves in z , \mathcal{F}_{xy} is the Fourier transform in x and y , and \mathcal{S}, \mathcal{J} are spreading and interpolation matrices. Since \mathcal{M} is symmetric, it should be the case that $\mathcal{J}^* = \mathcal{S}$ (w.r.t L_2 inner product). Currently, if we spread torque with the derivatives of the kernel (as in Eq. 6.2), the angular velocity is computed by interpolating the curl of the linear velocity with the kernel. This means $\mathcal{J}^* \neq \mathcal{S}$.

From Eq. 1.9, the definition/properties of convolution, and the fact that the velocity and kernel are in L_2 , we find that the angular velocity of a particle at \mathbf{y} can be interpolated with

$$\Omega(\mathbf{y}) = \frac{1}{2}(\nabla_{\mathbf{x}} \times \mathbf{u}(\mathbf{x})) \circledast \Delta_{\tau}(\mathbf{x}) = \frac{1}{2}\nabla_{\mathbf{y}} \times (\mathbf{u}(\mathbf{x}) \circledast \Delta_{\tau}(\mathbf{x})). \quad (6.9)$$

The discretization of the integral in Eq. 6.9 on a grid G which is uniform in x, y and Chebyshev in z (with weights ξ_z) is given by

$$\Omega(\mathbf{y}_k) = -\frac{h_{xy}^2}{2} \sum_{\mathbf{x} \in G} \nabla_{\mathbf{y}} \times (\mathbf{u}(\mathbf{x}) \Delta_{\tau}(\mathbf{x} - \mathbf{y}_k)) \xi_z(\mathbf{x}) = -\frac{h_{xy}^2}{2} \sum_{\mathbf{x} \in G} \begin{pmatrix} w(\mathbf{x}) \partial_y - v(\mathbf{x}) \partial_z \\ u(\mathbf{x}) \partial_z - w(\mathbf{x}) \partial_x \\ v(\mathbf{x}) \partial_x - u(\mathbf{x}) \partial_y \end{pmatrix} \Delta_{\tau}(\mathbf{x} - \mathbf{y}_k) \xi_z(\mathbf{x}) \quad (6.10)$$

This is the weighted adjoint of the operation in Eq. 6.3 (or compare with the second term in Eq. 1.6). Note the negative sign, which makes sense given that the derivative operator in L_2 is formally skew-symmetric.

In the following figures, we show that we can reduce the asymmetry previously observed between trans-rot and rot-trans by interpolating the linear velocity with the curl of the kernel.

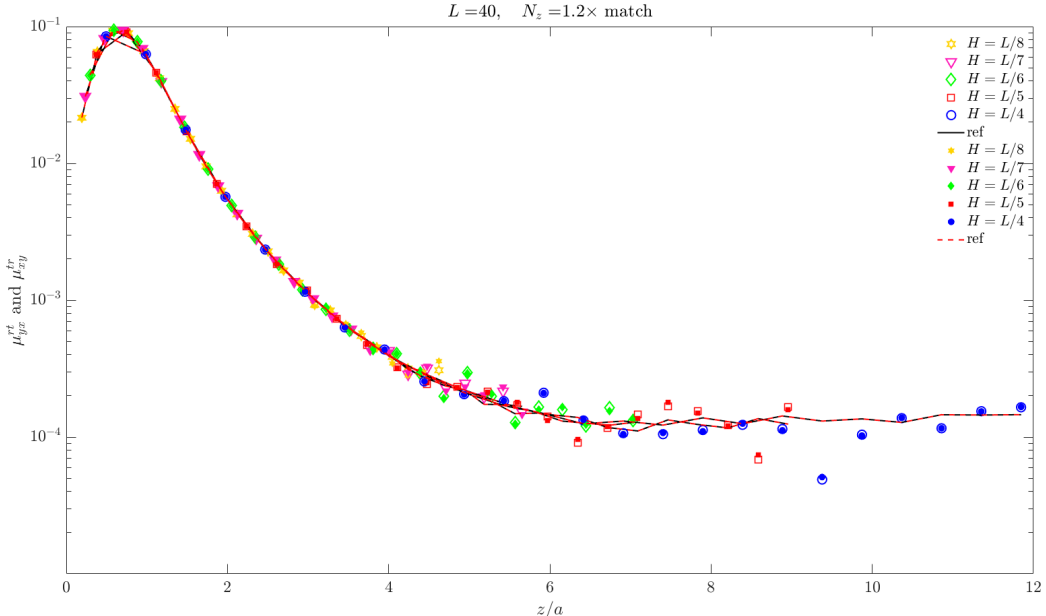


Figure 30: Rot-trans (unfilled) and trans-rot (filled) self mobility for $L = 40$ and fixed `fac` as H is increased. Reference results for rot-trans are the solid black lines, and those for trans-rot are the dashed red lines. We calculate the angular velocity using Eq. 6.10, i.e. we interpolate with the derivatives of the kernel.

Comparing Figure 28 with Figure 30 indicates that we have, in fact, improved the asymmetry by interpolating with the correct adjoint of spreading. There is better agreement in the results for $N_z = 1.2 \times$ match as well as the references. This is further confirmed in Figure 31, which shows a more rapid decrease in absolute asymmetry as points are added to the Chebyshev grid, in comparison to Figure 29.

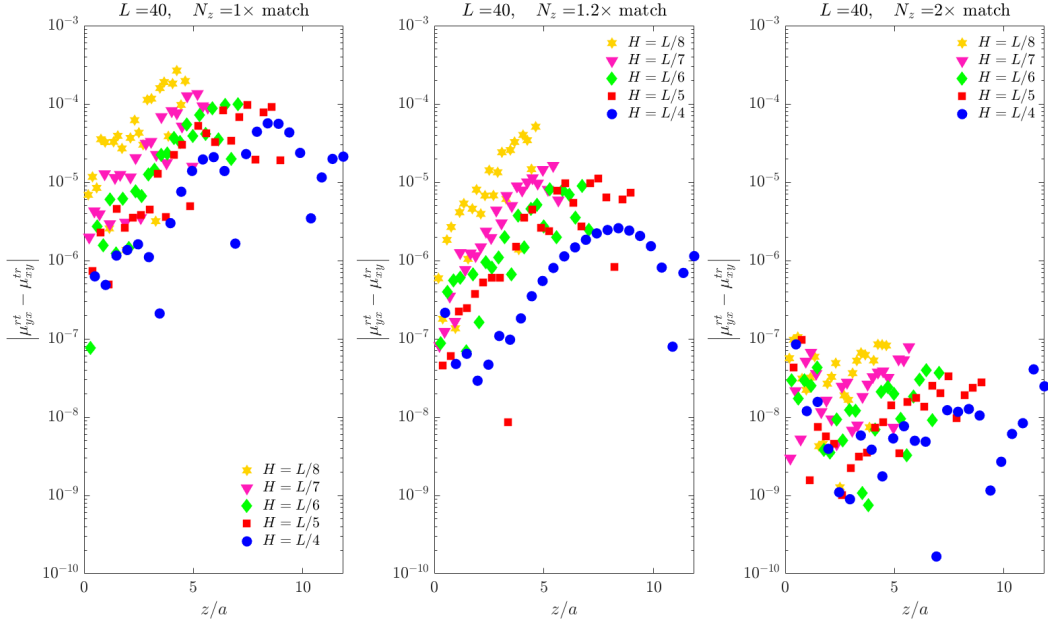


Figure 31: Absolute asymmetry in rot-trans for $L = 40$ and fixed `fac` as H is increased. We compute the rotational velocity with Eq. 6.10, i.e. we interpolate with the derivatives of the kernel.

6.2 Robustness of other mobilities in bottom wall and slit channel

Here, we confirm that using $N_z = \text{match } h_{xy}$ gives reasonable results for the other mobility components in the bottom wall and slit channel geometries. In all of the following figures, $h_{xy} = 0.4$, and the reference results (solid lines) are computed on a doubled grid in each direction (with double spreading width). While only results for $L = 40$ are shown, I've confirmed similar results for several $L < 40$.

6.2.1 Rot-rot in bottom wall

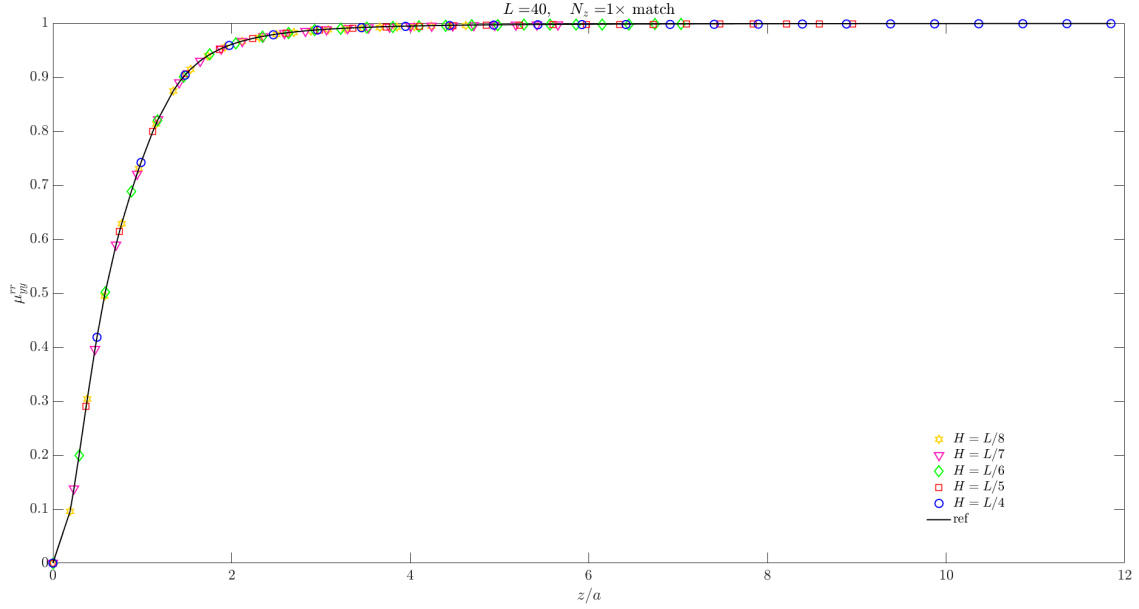


Figure 32: Rot-rot self mobility in the bottom wall geometry for $L = 40$ and several positions of the open boundary.

6.2.2 Trans-trans in bottom wall

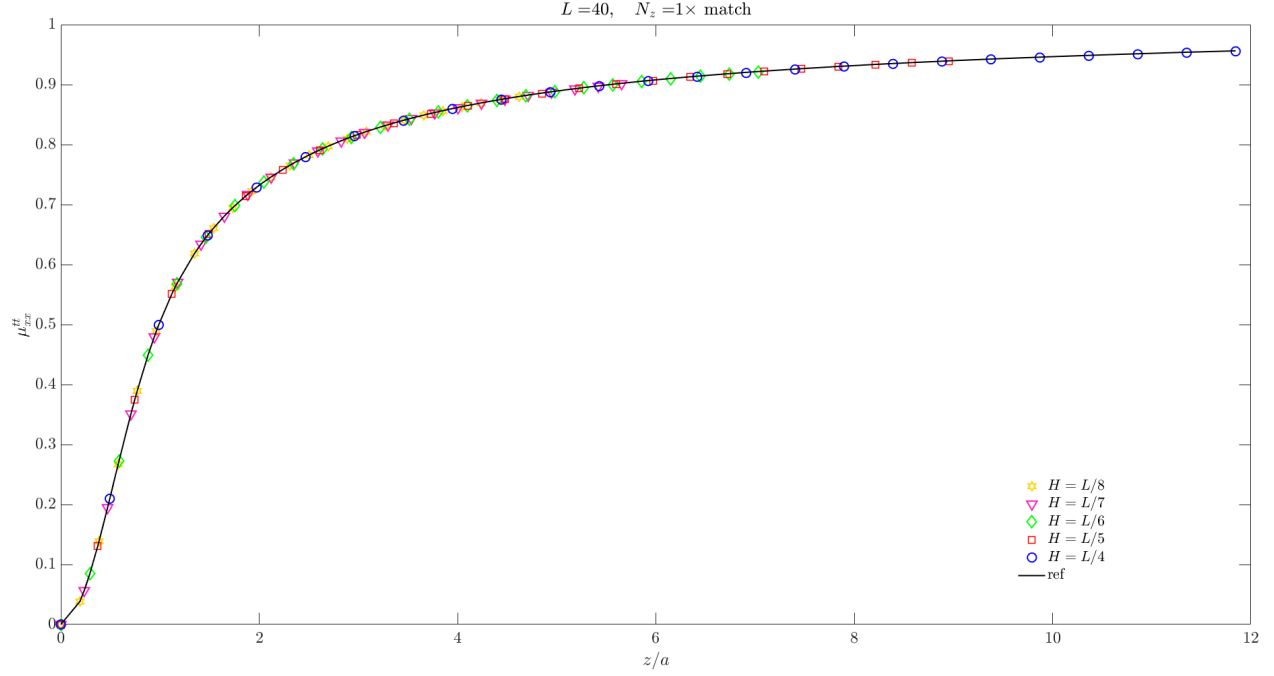


Figure 33: Trans-trans self mobility in the bottom wall geometry for $L = 40$ and several positions of the open boundary.

6.2.3 Trans-rot in slit channel

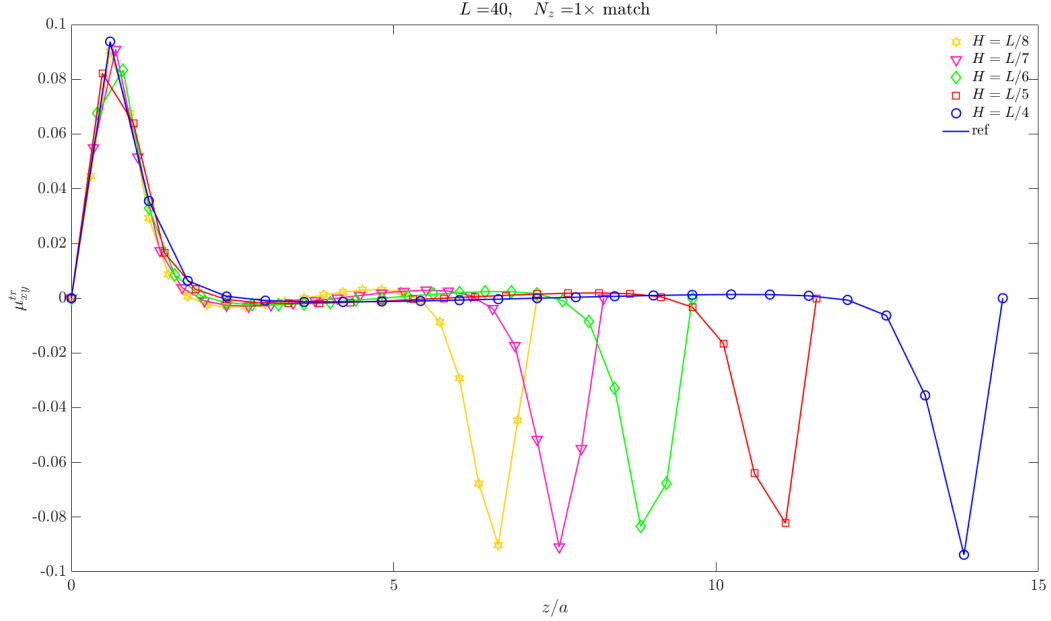


Figure 34: Trans-rot self mobility in the slit channel geometry for $L = 40$ and several channel heights.

6.2.4 Rot-trans in slit channel

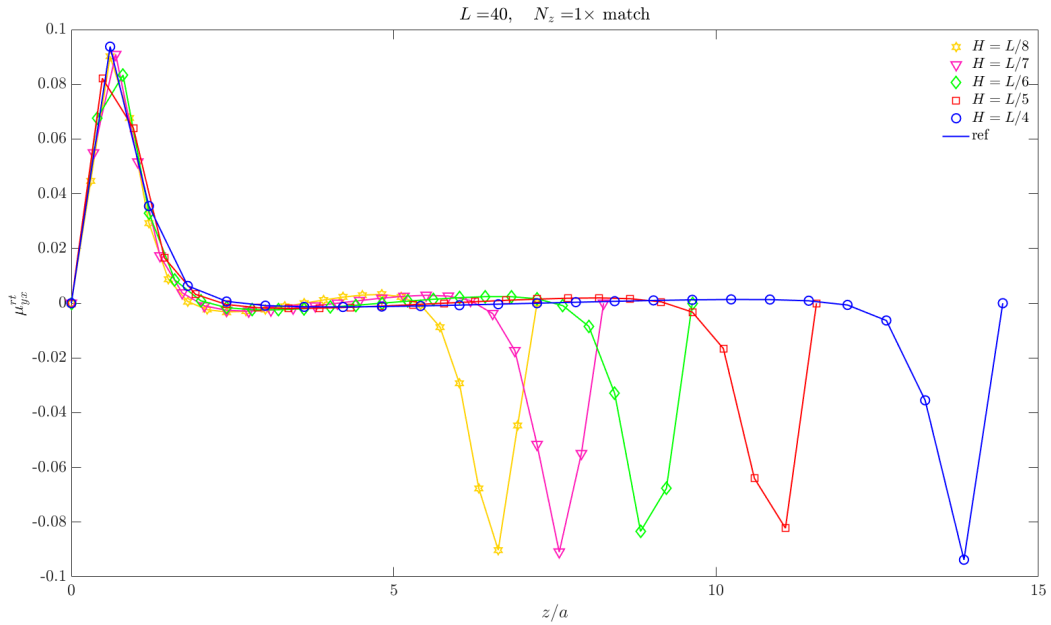


Figure 35: Rot-trans self mobility in the slit channel geometry for $L = 40$ and several channel heights.

6.2.5 Asymmetry between rot-trans and trans-rot in slit channel

In Figure 36, we show the absolute asymmetry between the two mobility calculations, given by $|\mu_{yx}^{rt} - \mu_{xy}^{tr}|$. We also compare asymmetries when interpolating the curl of velocities with kernel and interpolating the velocities with the derivatives of the kernel, as described in Section 6.1.4. Similar to the bottom wall, using the adjoint of spreading for interpolation gives better symmetry.

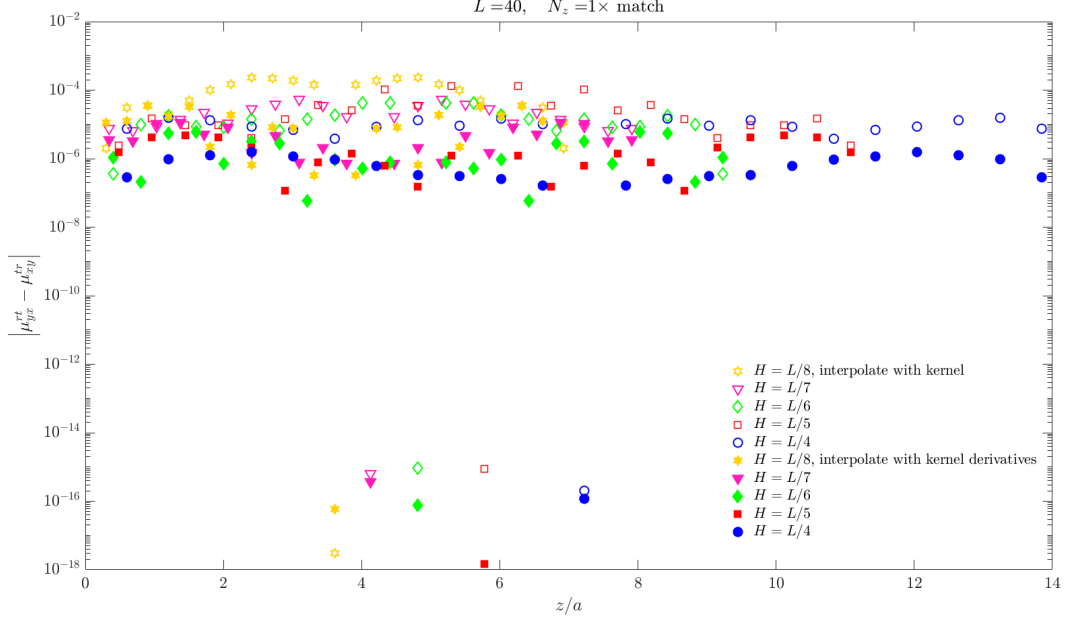


Figure 36: Slit channel absolute asymmetry in rot-trans for $L = 40$ and $\text{fac}=1$ as H is increased. The unfilled markers correspond to interpolating the curl of velocities with the kernel, and filled markers are from interpolating velocities with derivatives of the kernel.

6.2.6 Rot-rot in slit channel

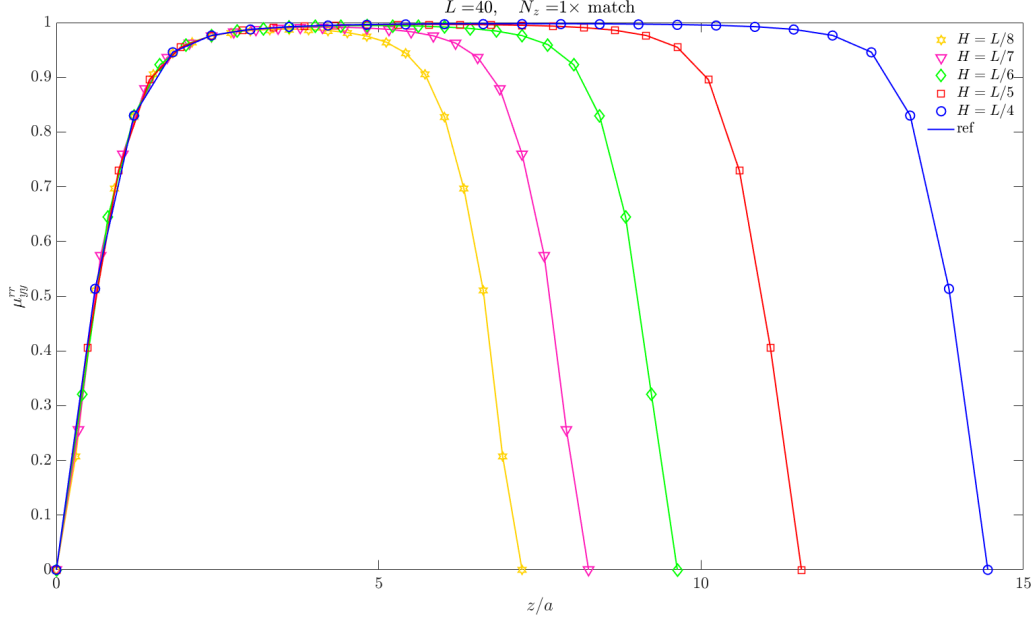


Figure 37: Trans-trans self mobility in the slit channel geometry for $L = 40$ and several channel heights.

6.2.7 Trans-trans in slit channel

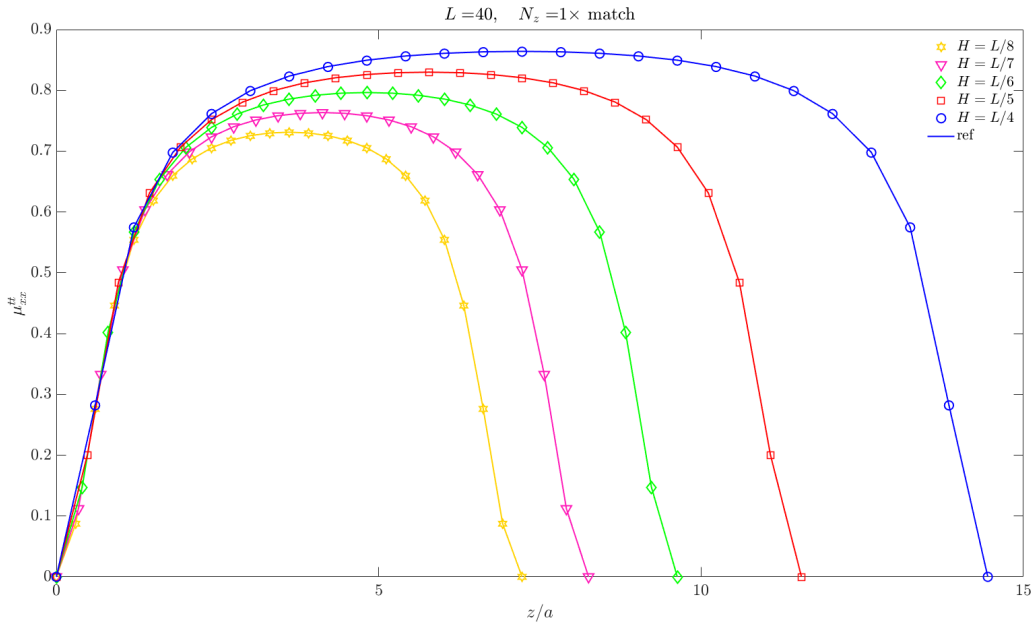


Figure 38: Trans-trans self mobility in the slit channel geometry for $L = 40$ and several channel heights.

7 Spreading and interpolation through a uniform z grid

In order to leverage the FINUFFT library, in which efficient spreading and interpolation routines have been implemented, the z grid must be uniform with the same spacing as the grid in xy . Here, we describe the process of going through a uniform grid, and check whether using such a spacing in z preserves accuracy and robustness of particle mobilities in the bottom wall and slit channel geometries using $w_f = w_\tau = 6$ (TLDR: it doesn't).

Suppose that we select a factor `aspect` such that the upper boundary is at $H = L/\text{aspect}$ (generally, `aspect` ≥ 4). Let the required grid spacing in z be h_z . Then, we adjust the upper endpoint to $H = h_z \left\lfloor \frac{L}{h_z \cdot \text{aspect}} \right\rfloor$ so that the grid from 0 to H with spacing h_z includes the endpoints. We interpolate quantities at points z_j^u on the uniform grid to points z_i^c on a Chebyshev grid *with middle spacing matching h_z* using a nearest-neighbor Lagrange interpolant;

$$(\mathbf{I}_{u2c})_{ij} = \prod_{\substack{k \neq j \\ |z_j^u - z_k^u| < \frac{nh_z}{2}}} \frac{z_i^c - z_k^u}{z_j^u - z_k^u}, \quad (7.1)$$

where n is the support of the local interpolant. In practice, we take $n = \frac{w_m h_{xy}}{h_z}$. In order to accurately interpolate near the endpoints, we extend the uniform grid with $\lfloor n/2 \rfloor$ points to the left of 0 and $\lceil n/2 \rceil$ points to the right of H . Then, for each point in the xy -plane, we interpolate the slice $\mathbf{f}^{xy}(z^u)$ from the uniform to Chebyshev grid through $\mathbf{f}^{xy}(z^c) = \mathbf{I}_{u2c}\mathbf{f}^{xy}(z^u)$.

Similarly, in order to transform $\mathbf{C}_{\hat{f}^{xy}}$ from the Fourier-Chebyshev domain back to the uniform grid, for each wave number k_x, k_y , we evaluate the Chebyshev interpolant using Chebyshev polynomials on the uniform (and unextended) z grid and the slice of Chebyshev coefficients. This yields $\hat{\mathbf{f}}^{xy}(z^u)$, i.e. the Fourier coefficients corresponding to k_x, k_y along the uniform z grid. Then, for each z_j^u , we compute the 2D inverse FFT to transform back to real space and obtain $\mathbf{f}^{xy}(z^u)$ for all x, y .

In the following sections/figures, the setup is identical to that used in [Sections 6.1.1 - 6.2.7](#) with the exception that we always spread torque and interpolate angular velocity with the derivatives of the ES kernel. Note, I also tried spreading torque with the spectral evaluation method (no kernel derivatives), though the results aren't very different. Reference mobilities are computed on grids with double the resolution in each direction.

I believe that all the issues we'll observe are, in part, a result of slow convergence of the interpolation between the uniform and Chebyshev grid due to truncation/smoothness of the kernel.

7.1 Trans-rot and rot-trans coupling in bottom wall using a uniform z grid

Comparing [Figures 39 - 40](#) to [Figures 22 - 25](#), we see that a larger value of `fac = 1.8` is required to reduce the oscillations. Also, comparing [Figure 41](#) to [Figure 31](#), we note that symmetry is not as well maintained.

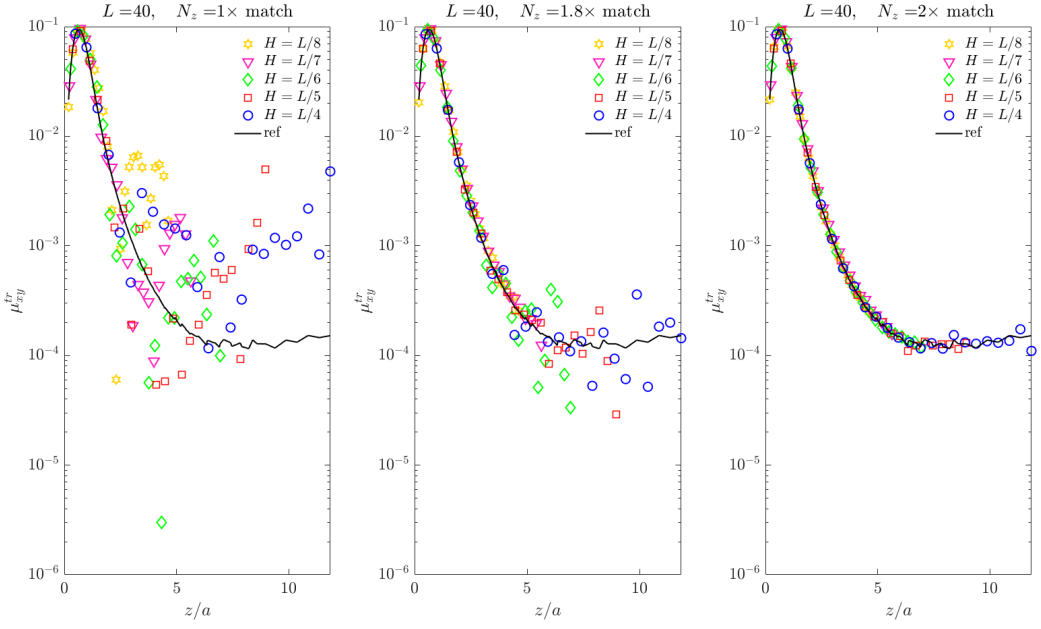


Figure 39: Trans-rot self mobility for $L = 40$ and fixed `fac` as H is increased. Here, we spread onto a uniform grid in each direction, interpolate onto the Chebyshev grid in z , solve the BVP, and interpolate back onto the uniform grid in z .

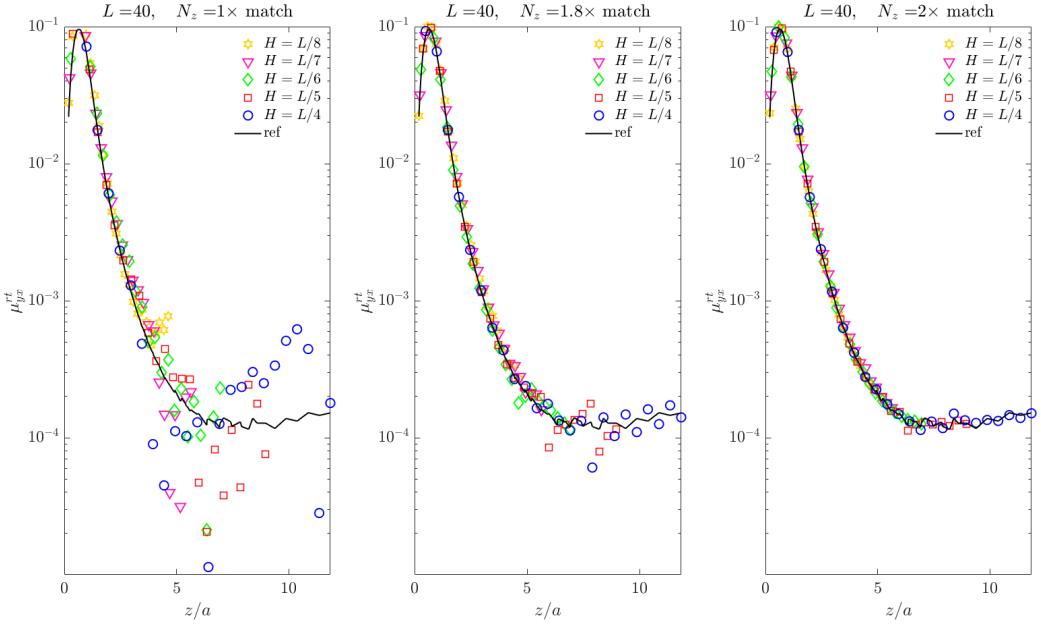


Figure 40: Rot-trans self mobility for $L = 40$ and fixed `fac` as H is increased. Here, we spread onto a uniform grid in each direction, interpolate onto the Chebyshev grid in z , solve the BVP, and interpolate back onto the uniform grid in z .

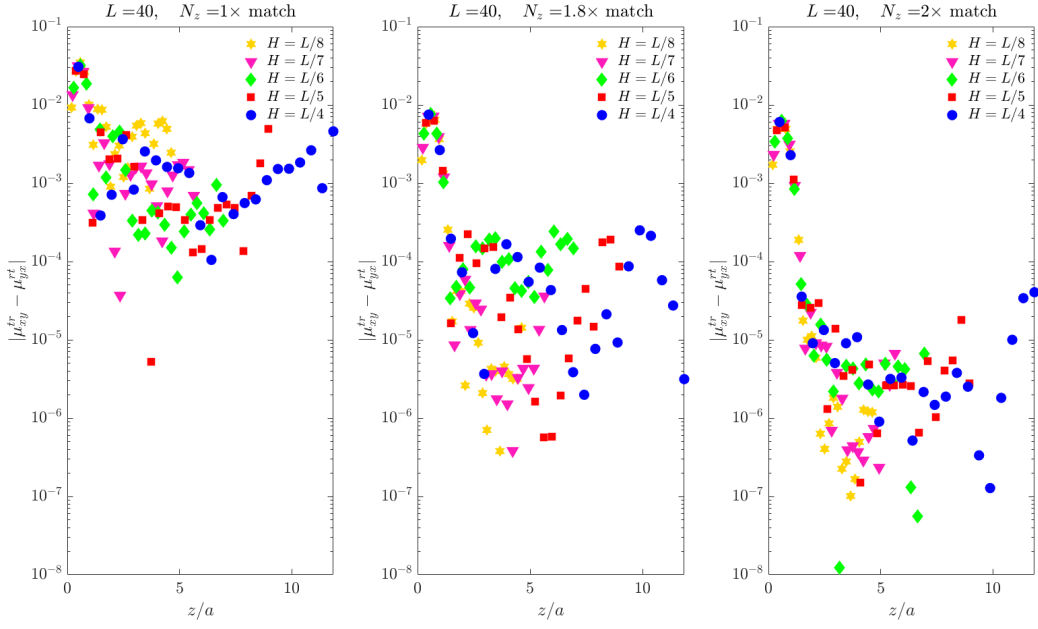


Figure 41: Absolute asymmetry in rot-trans for $L = 40$ and fixed `fac` as H is increased. Here, we spread onto a uniform grid in each direction, interpolate onto the Chebyshev grid in z , solve the BVP, and interpolate back onto the uniform grid in z .

7.2 Rot-rot and trans-trans coupling in bottom wall using a uniform z grid

Figures 42 - 43 show at least two problems in comparison to Figures 32 - 33. First, and most glaringly, the combined references from each aspect ratio don't produce a smooth reference curve. The position of the open boundary shouldn't affect the mobility at a given height above the wall.

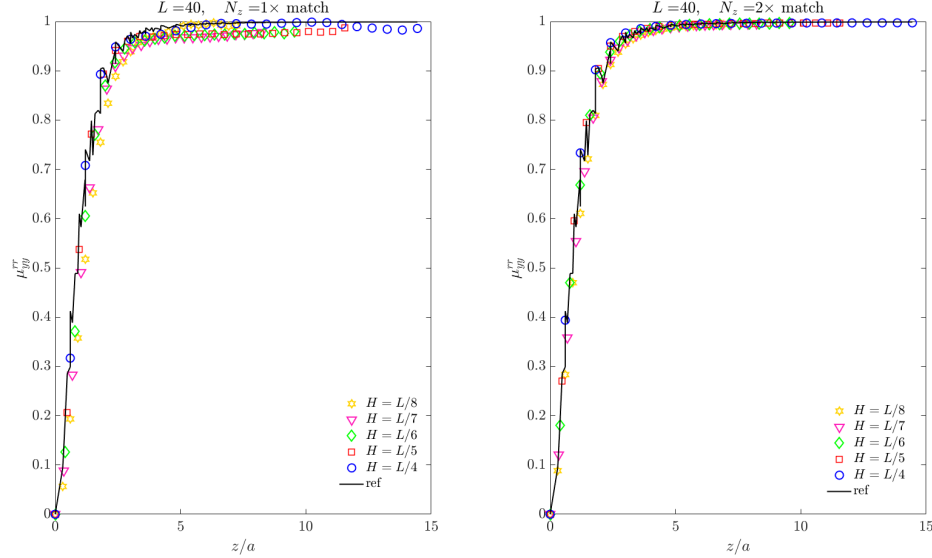


Figure 42: Rot-rot self mobility in the bottom wall geometry for $L = 40$ and several positions of the open boundary. Here, we spread onto a uniform grid in each direction, interpolate onto the Chebyshev grid in z , solve the BVP, and interpolate back onto the uniform grid in z .

Second, we require upsampling in z to better match the reference results, while this was not required when we spread directly onto the Chebyshev grid.

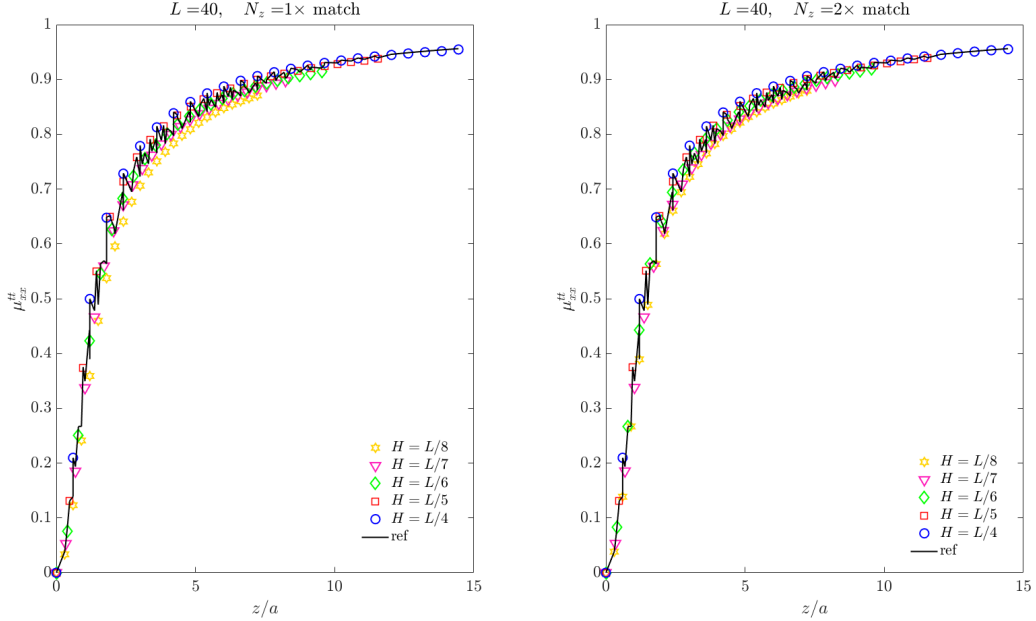


Figure 43: Trans-trans self mobility in the bottom wall geometry for $L = 40$ and several positions of the open boundary. Here, we spread onto a uniform grid in each direction, interpolate onto the Chebyshev grid in z , solve the BVP, and interpolate back onto the uniform grid in z .

7.3 Trans-rot and rot-trans coupling in slit channel using a uniform z grid

As before, we see that we require upsampling in z to match the reference results, while this is not required when we spread directly onto the Chebyshev grid. Moreover, Figures 44 - 45 highlight the effect of ES kernel settings. From Figure 17, we know that the dipole kernel with $w_\tau = 6$ is less smooth than the corresponding monopole kernel of the same width. In Figure 44, we spread forces onto the uniform grid with the monopole kernel and interpolate onto the Chebyshev grid. However, when we interpolate the fluid velocity from the Chebyshev grid back to the uniform grid, we use the derivatives of the dipole kernel. This is where more of the error is made, and is why the rot-trans mobility requires upsampling to converge to the reference result.

On the other hand, in Figure 45, we spread the curl of the torques onto the uniform grid with the dipole kernel and interpolate onto the Chebyshev grid. So, more of the error is made during spreading, rather than when going back to the uniform grid; and, it explains why the trans-rot mobility matches the max and min of the reference but is less regular within the channel.

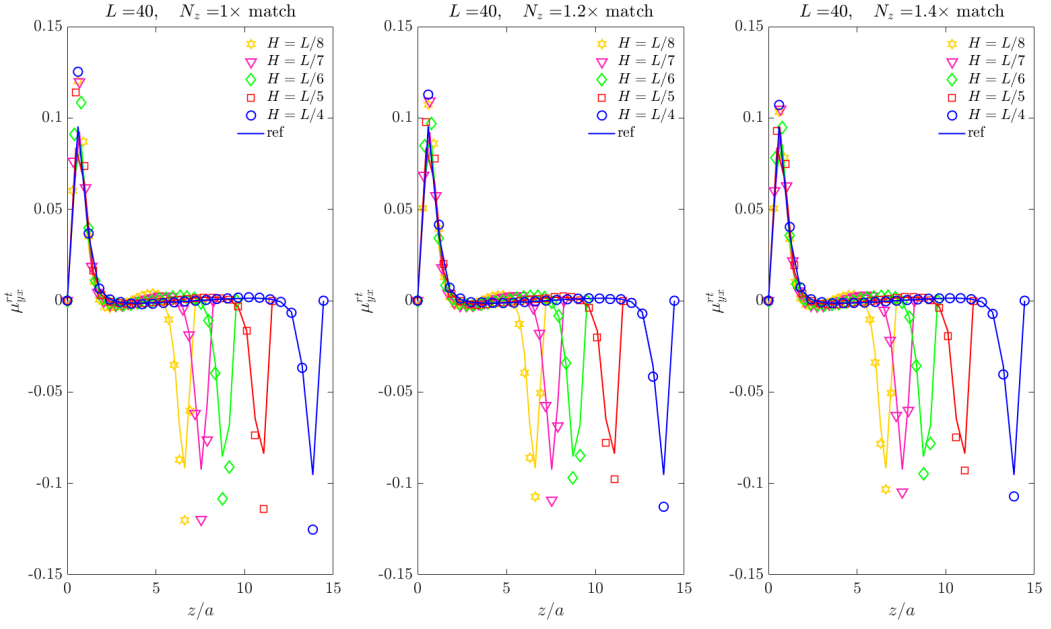


Figure 44: Rot-trans self mobility in the slit channel geometry for $L = 40$ and several channel heights. Here, we spread onto a uniform grid in each direction, interpolate onto the Chebyshev grid in z , solve the BVP, and interpolate back onto the uniform grid in z .

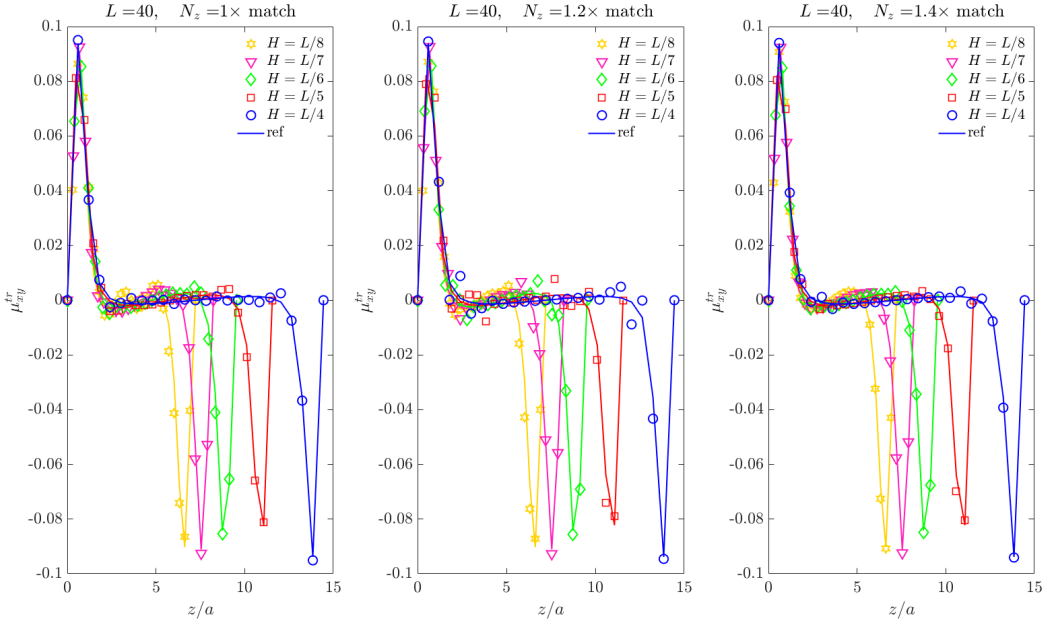


Figure 45: Trans-rot self mobility in the slit channel geometry for $L = 40$ and several channel heights. Here, we spread onto a uniform grid in each direction, interpolate onto the Chebyshev grid in z , solve the BVP, and interpolate back onto the uniform grid in z .

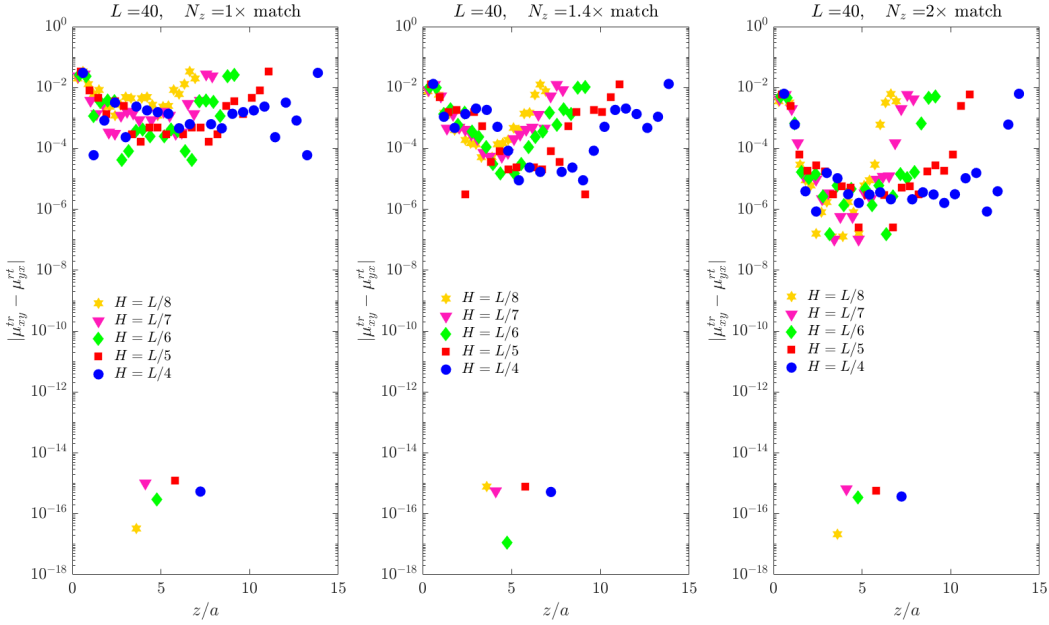


Figure 46: Slit channel absolute asymmetry in rot-trans for $L = 40$ and `fac=1` as H is increased. Here, we spread onto a uniform grid in each direction, interpolate onto the Chebyshev grid in z , solve the BVP, and interpolate back onto the uniform grid in z .

7.4 Rot-rot and trans-trans coupling in slit channel using a uniform z grid

From our previous observations, the requirement of upsampling for rot-rot, and the absence thereof for trans-trans can be explained by the smoothness of the monopole kernel over that of the dipole.

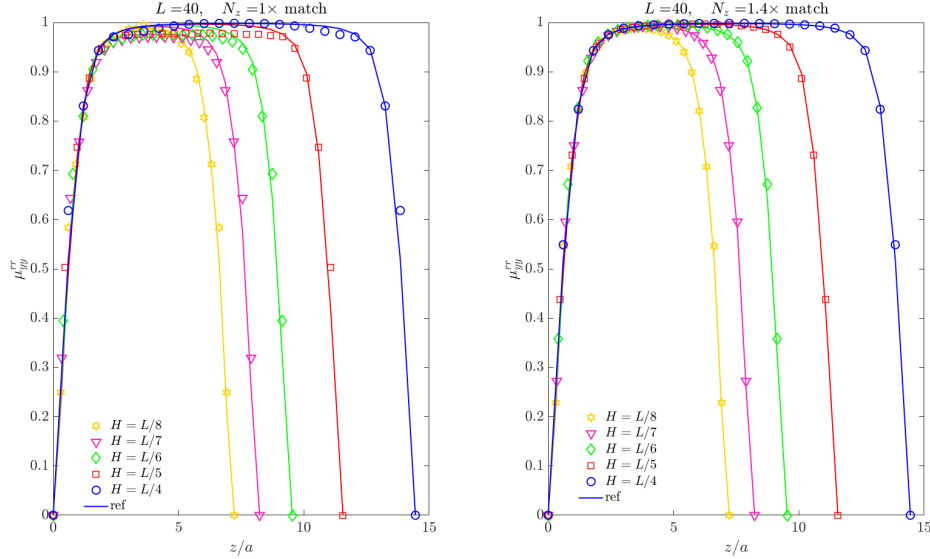


Figure 47: Rot-rot self mobility in the slit channel geometry for $L = 40$ and several channel heights. Here, we spread onto a uniform grid in each direction, interpolate onto the Chebyshev grid in z , solve the BVP, and interpolate back onto the uniform grid in z .

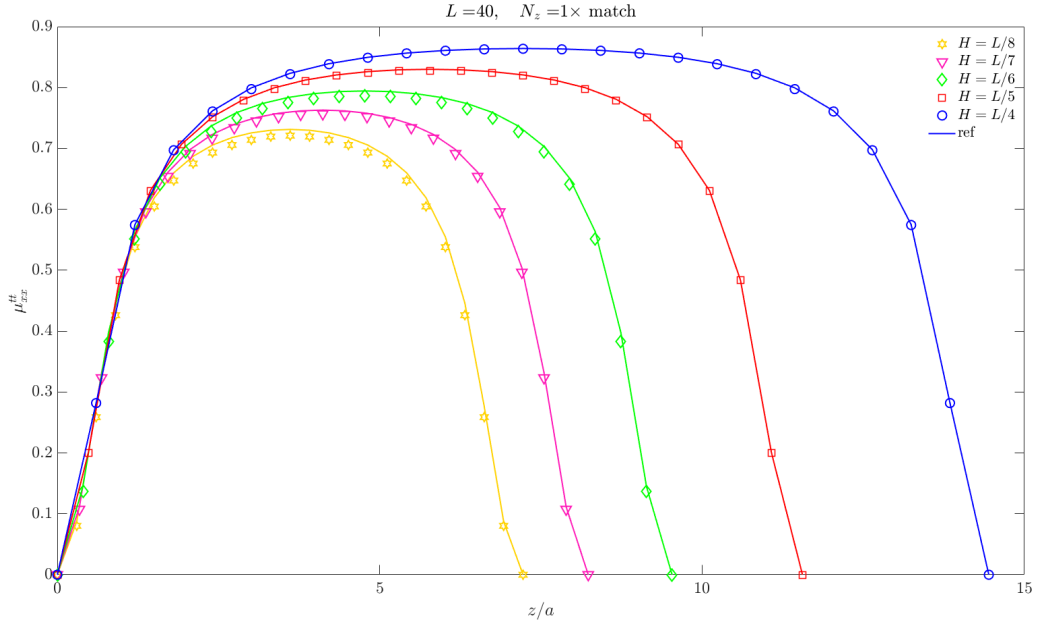


Figure 48: Trans-trans self mobility in the slit channel geometry for $L = 40$ and several channel heights. Here, we spread onto a uniform grid in each direction, interpolate onto the Chebyshev grid in z , solve the BVP, and interpolate back onto the uniform grid in z .

8 For posterity

In [Table 4](#), we report extrapolated radii and associated error obtained using Peskin's standard 3-point and 4-point kernels, as well as the new 5-point and 6-point kernels [8].

Table 4: Percent error for monopole and dipole radii fits using Peskin's kernels

w	3	4	5	6
radii	1.0505	1.3160	1.2640	1.5206
%-error	35.2570	1.1453	0.7533	0.0471

(a) Peskin Monopole

w	3	4	5	6
radii	0.73669	1.7513	1.5267	2.6712
%-error	4.16	0.888	0.204	0.0456

(b) Peskin Dipole

References

- [1] Sune Lomholt and Martin Maxey. Force-coupling method for particulate two-phase flow: Stokes flow. *Journal of Computational Physics*, 184:381–405, 01 2003.
- [2] L. Greengard. Spectral integration and two-point boundary value problems. *SIAM Journal on Numerical Analysis*, 28(4):1071–1080, 1991.
- [3] Luc P. Faucheux and Albert J. Libchaber. Confined brownian motion. *Phys. Rev. E*, 49:5158–5163, Jun 1994.
- [4] Steven Delong, Florencio Balboa Usabiaga, and Aleksandar Donev. Brownian dynamics of confined rigid bodies. *The Journal of Chemical Physics*, 143, 06 2015.
- [5] James Swan and John Brady. Simulation of hydrodynamically interacting particles near a no-slip boundary. *Physics of Fluids*, 19, 11 2007.
- [6] Alex H. Barnett, Jeremy F. Magland, and Ludvig af Klinteberg. A parallel non-uniform fast fourier transform library based on an "exponential of semicircle" kernel, 2018.
- [7] H. Hasimoto. On the periodic fundamental solutions of the stokes equations and their application to viscous flow past a cubic array of spheres. *Journal of Fluid Mechanics*, 5(2):317328, 1959.
- [8] Yuanxun Bao, Jason Kaye, and Charles S. Peskin. A gaussian-like immersed-boundary kernel with three continuous derivatives and improved translational invariance. *Journal of Computational Physics*, 316:139144, Jul 2016.